MICROLENSES AND MICROCAMERAS FOR BIOMEDICAL IMAGING

By

Aditi Kanhere

A dissertation submitted in partial fulfillment of
the requirements for the degree of

Doctor of Philosophy
(Electrical and Computer Engineering)

at the

UNIVERSITY OF WISCONSIN – MADISON

2015

Date of final oral examination: 8/12/2015

The dissertation is approved by the following members of the Final Oral Committee:
Hongrui Jiang, Professor, Electrical and Computer Engineering
Yu Hen Hu, Professor, Electrical and Computer Engineering
Zongfu Yu, Assistant Professor, Electrical and Computer Engineering
Justin Williams, Professor, Biomedical Engineering
Charles Heise, Professor, Surgery

Acknowledgements

This thesis would not be complete without many people in my life who believed in me, mentored me and encouraged me, without whom I could have never achieved this goal in my life. Hongrui Jiang has been more than a mere Principal Investigator. I have learnt so much from him in these past five years – the value of work discipline, the humility to respect your subordinates, virtue of strong leadership without micromanagement and most of all the passion to pursue science. If I ever got a chance to do my PhD all over again, I would do a lot of things differently but I would still ask to be mentored by Hongrui. Working in his research group has been an incredibly rewarding experience. I am sure I will continue to reap the benefits of the lessons learnt here in my professional life for several years to come. I am also grateful for the thoughtful and supportive questioning and assistance from my Ph.D. committee members at UW-Madison (Dr. Zhongfu Yu, Dr. Yu Hen Hu, Dr. Charles Heise, Dr. Justin Williams).

Bader Aldadali, Ye Liu, Chenhui Li, Chi-Chieh Huang, Kari Van Grinsven, Jayer Fernandes, Alireza Ousati Ashtiani, Hewei Liu, Hao Bian, Xuezhen Huang, Xiudong Wu, Yousuf Almoallem, Mohammad Moghimi, Xi Zhang and Yinggang Huang – my heartfelt thanks to all the MNSA team members. A special mention for Guangyun Lin for her able guidance throughout my second project. The countless brainstorming discussions over coffee, long hours spent doodling on the white board to solve research problems and most of all an empathetic ear whenever I need one – they have been there through all the phases of the journey.

I would like to take this opportunity to acknowledge the role of UW-Madison research facilities that made this research possible: the College of Engineering Student Machine Shop and UW Rapid Prototyping Consortium for help with machining and 3D printing.

And finally the most important people in my life - my family. I do not have words to express my gratitude towards my parents' and my sister's love, hardwork and sacrifice that has made me who I am. The last and most special thanks is reserved for my husband, Mukul – I could not have done this without his understanding, support and encouragement.

Table of Contents

1 Introduction 1

1.1 Microlenses and microcameras 1

1.2 Laparoscopic imaging 2

1.3 3D Microscopy 4

2 Fixed-focus microcameras for laparoscopy 9

2.1 Introduction 9

2.2 Mechanism 10

2.3 Fabrication 11

2.4 Experimental results 14

3 Thermo-responsive tunable-focus liquid lenses 20

3.1 Introduction 20

3.2 Principle of operation 21

3.3 Design Considerations 23

3.4 Materials and fabrication techniques 24

3.4.1 Liquid-phase photopolymerisation 24

3.4.2 Thermo-responsive hydrogel - NIPAAm 25

3.5 Fabrication 27

3.6 Characterization 30

3.6.1 Focal Length measurements 30

3.6.2 Imaging performance 31

4 Tunable-focusing laparoscopic camera 37

4.1 Design considerations 42

4.2 Fabrication 44

4.3 Simulation and Characterization 45

4.4 Polarizer 48

4.5 Mechanical actuation assembly 51

4.6 Graphical User interface 53

4.7 Imaging results 54

5 Remote axial focusing using tunable lenses in 3D microscopy 61

5.1 Introduction 61

5.2 Principle of operation 62

5.3 Experimental 63

5.3.1 Optical configurations 63

5.3.2 Optical Setup 64

5.3.3 Optical modelling 66

5.4 Results and discussion 68

5.4.1 Lens Calibration 68

5.4.2 Characterization 69

5.4.3 Axial tuning 69

5.4.4 Field of View and Numerical Aperture 70

5.4.5 Aberrations and resolution 71

5.4.6 Evaluation of system – Live Cell imaging 73

6 Summary and future work 76

6.1 Current Work 76

6.2 Future Work 77

6.2.1 Laparoscopic imaging tool 77

5.2.2. Axial scanning in microscopy using tunable lenses 77

7 Publications 78

Table of Figures

Figure 2.1. Prototype of the micro camera array. (a) and (b) are 3D schematics of two different configurations of the camera array while (c) and (d) are corresponding photo images of these two configurations of the four-camera imaging system around a surgical port. 10

Figure 2.2 Batch fabrication process for all PDMS camera holders and bridges. This framework is critical for alignment of the four cameras symmetrically around the laparoscopy port and with each other. (a) Spacers on a glass slide are used to define thickness of poly-IBA structure. (b) Mask with spacers form a cavity filled with IBA. UV exposure is used to cure the IBA pre-polymer. (c) Poly-IBA mold for bridges and lens holders is formed. (d) Uncured PDMS is poured onto the poly-IBA mold and cured for 4 hours at 80oC. (e) Final PDMS camera holders and bridge structure. 13

Figure 2.3(a) – (d) Individual images captured by the four cameras placed in a configuration shown in Fig. 1(a) and (c). (e) The panorama obtained by stitching (a) - (d). 14

Figure 2.4(a) – (d) Individual images captured by the four cameras configured as shown in Fig. 1(b) and (d). 15

Figure 2.5. (a) Composite image obtained by stitching images from Fig. 3(a) - (d) and Fig. 4(a) - (d). (b) Image obtained by a 5mm zero-degree laparoscopic camera with same experimental parameters. Significant increase in the FoV is achieved in (a) as compared to (b). 16

Figure 3.1 Schematic representation illustrating the operation of a thermo-responsive tunable liquid lens. As the local temperature increases, the hydrogel releases water and contracts, thereby increasing the radius of curvature and decreasing the focal length of the water-oil lens. This focal length change is reversible. 22

Figure 3.2 Schematic of side profiles of concave and convex states of water-oil lens. When the water profile bulges out into the oil container, the water-oil lens becomes divergent. The minimum height of the oil container is determined by the maximum height of the protrusion of the lens into the container. Similarly, when the water-oil meniscus curves into the water container, the water-oil lens becomes convergent. The minimum height of the water container is therefore determined by the maximum dip of lens into the water container. 23

Figure 3.3 Hydrogel is cross-linked polymer chain attracted with external stimuli. It undergoes reversible volumetric transitions in response to changes in external environmental [24]. _____ *26*

Figure 3.4 Fabrication process flow for thermo-responsive hydrogel based tunable liquid lenses _____ *29*

Figure 3.5 Focal lengths of microlenses plotted against temperatures for initial water volumes of 1.25 μL, 1.5 μL, and 1.7 μL filled in the liquid lenses. 1.5 μL water containers yielded an optimum focal length range when the temperature was varied from 42^0C to 75^0C. _____ *31*

Figure 3.6 Image of the 1951 USAF resolution target as seen by a microlens with a focal length of 20 mm. The smallest resolvable features are element 3 in group 3 corresponding to a resolution of 10.10 line pairs/mm. 32

Figure 3.7 Simulated and experimental normalized light intensity profiles obtained by imaging a laser beam focused by microlenses at focal lengths (a) 20 mm (b) 40 mm and (c) 50 mm. The corresponding spherical aberration values shown in the table are calculated as the full width at half maximum. _____ *33*

Figure 4.1. An overview of the key elements of a laparoscopic surgery [2] _____ *37*

Figure 4.2 Schematic representation of (a) our system, as implemented in a multi-port laparoscopic surgery. (b) The cross-sectional view of an integrated trocar-camera assembly after insertion within an abdominal cavity. (c)-(d) The reconfigurability of camera perspectives using an umbrella-like mechanical actuator. _____ *38*

Figure 4.3 (Top) A three dimensional representation of the assembly of a microcamera unit. Every camera module comprises of a commercial image sensor (1 mm × 1 mm) , a tunable thermo-responsive liquid lens with an integrated heater-sensor and a polarizer. (Bottom) An image of one microcamera shown for scale next to a US penny. _____ *41*

Figure 4.4 Schematic of the integrated microheater-sensor design. The coil track shown in black is the microheater; whereas the coil shown in red the temperature sensor. The width of the coil track is 0.2 mm whereas its thickness is 200 nm. _____ *42*

Figure 4.5 Fabrication process flow for aluminum micro heater coil patterned on PDMS using lift-off process _____ *44*

Figure 4.6 Simulation results for temperature of the microheater at time t=1 s for actuation voltages of 200 mV, 250 mV and 300 mV. The heat is localized and uniformly distributed in the heating element within a tolerance of 6.66%. _____ *46*

Figure 4.7 Calibration curves for heater and sensor resistances _____ *47*

Figure 4.8 Calibration curves for heater and sensor resistances _____ *49*

Figure 4.9 Selective transmission of a linearly polarized He-Ne laser (λ=630 nm) when passed through the polarizer. _____ *50*

*Figure 4.10. Crankshaft actuator design calculations*_____ *51*

Figure 4.11 Different parts of the trocar-camera assembly. (Inset) shows a close-up of the dc motor with a two-stage gear reduction set. _____ *52*

*Figure 4.12 (a-b) Actuation of the TCA. As the crank rotates clockwise, the connecting rod pulls the runner downwards. As the runner slides down the trocar, the stretchers pull the arms closer to the trocar.*_____ *53*

Figure 4.13 Reduction in glare with the use of a polarizer as seen from comparison of an image without using a polarizer in front of a tunable camera (left) and the same image captured with a polarizer in front of the lens (right). _____ *54*

Figure 4.14 Images of a test scene as captured by a single camera while the focal length of its tunable liquid lens was being tuned using a microheater. _____ *55*

Figure 4.15 Images of a mimicked surgical scene as captured by our camera array. (a-d) Sharp images of all the sub scenes were obtained by individual cameras These scenes were then stitched together in a commercial software, PTGui™ to obtain a very large field of view compared to any single camera alone (e). _____ *56*

Figure 4.16 (a) Pixel intensity distribution (histogram) of the panoramic image in Fig. 16 (e). (b) Cropped panoramic image before processing (c) Cropped panoramic image after redistribution of the intensity levels in the histogram. _____ *58*

Figure 4.17 Enhanced depth perception due to multi-camera array. Images of two tubes (Ø=15 mm) separated by a distance of 10 mm, as captured by four cameras in the TCA. Imaging the same object with a multi-camera array yields depth cues from four different viewing perspectives, leading to an enhanced depth perception compared to any single camera alone. _____ *59*

Figure 5.1 Non-telecentric systems cause change in magnification and hence field of view during axial scanning whereas the field of view is maintained constant in a telecentric optical setup [11]. _____ *63*

Figure 5.2 An optical ray tracing diagram of the setup of our 3D microsope. A 0.81mm diameter He-Ne laser beam is first expanded by a 9x beam expander before being deflected onto a tunable lens-objective combination that focuses the light at different depths of a sample depending upon the focal length of the tunable lens. The detection arm consists of a tube lens which focuses light to produce an image on an image sensor. _____ *65*

Figure 5.3 A 3D representation of the actual optical setup of the 3D microscope with remote axial focusing achieved by a tunable liquid lens placed close to the rear stop of a microscope objective. _____ *66*

Figure 5.4 A shaded model drawing of a 3D layout of a tunable liquid lens and a commercial microscope objective, as designed in ZEMAX optical modelling software. _____ *67*

Figure 5.5 3D schematics of batch fabrication molds used in the fabrication of lens containers. These molds were 3D printed using stereolithography.; _____ *68*

Figure 5.6 Plot showing the variation of the focal length with respect to the ambient temperature of a tunable liquid lens. As the temperature is varied from 30 degrees to 90 degrees , the lens tunes from concave focal lengths of -30mm to -∞, then switches to a convex lens from focal lengths of +∞ to 45mm. _____ *69*

Figure 5.7 ZEMAX simulations showing the axial shift of the native focal plane with a change in the focal length of the tunable lens _____ *70*

Figure 5.8 A plot of the Modulation Transfer Function as derived from ZEMAX for various tunable lens focal lengths. A reasonable contrast of more than 20% is observed for spatial frequencies above 200 cycles/mm. _ *71*

Figure 5.9 Demonstration of axial focusing of the 3D microscope using a microfluidic channel. (a) Schematic of the microfluidic device used for imaging. It consists of 2 layers of microfluidic channels with microspheres flown through them. (b) shows images of the 20 µm beads in the lower channel (c)-(d) shows focusing on multiple layers within the top microfluidic channel containing 40 µm beads _____ *72*

Figure 5.10 Images of SF21 cells as captured by our 3D microscope along different axial positions of the focal plane. _____ *73*

Abstract

Liquid lens technology is a rapidly progressing field driven by the promise of low cost fabrication, faster response, fewer mechanical elements, versatility and ease of customization for different applications. Here we present the use of liquid lenses for biomedical optics and medical imaging. I will specifically focus on our approaches towards the development of two liquid-lens optical systems – laparoscopic cameras and 3D microscopy.

The first part of this work is based on the development of a multi-camera laparoscopic imaging system with tunable focusing capability. The work attempts to find a solution to overcome many of the fundamental challenges faced by current laparoscopic imaging systems. The system is developed upon the key idea that widely spread multiple, tunable microcameras can cover a large range of vantage points and field of view (FoV) for intra-abdominal visualization. Our design features multiple tunable-focus microcameras integrated with a surgical port to provide panoramic intra-abdominal visualization with enhanced depth perception. Our system can be optically tuned to focus in on objects within a range of 5 mm to ∞, with a FoV adjustable between 36^0 and 130^0. This unique approach also eliminates the requirement of an exclusive imaging port and need for navigation of cameras between ports during surgery.

The second part of this report focuses on the application of tunable lenses in microscopy. Conventional wide-field microscopy is one of the most widely used optical microscopy technique. This technique typically captures a two dimensional image of a specimen. For a volumetric visualization of the sample or to enable depth scanning along the axial direction, it is necessary to move the sample relative to the fixed focal plane of the microscope objective. For this purpose, a mechanical z-scanning stage is typically employed. The stage enables the focal plane to move

through the sample. Typical approaches used to achieve axial scanning are a motorized stepper stage or a piezoelectric stage. While stepper motors offer the advantage of unlimited travel distance, they suffer from hysteresis. Piezoelectric stages on the other hand, help eliminate hysteresis at the cost of the travel distance which is reduced to 100-200 μm. Both the types of stages, however, are bulky and cause vibrations and wobble in the sample due to high inertia. Additional care is required to avoid mechanical overshoots and backlash from the tip touching the sample. Additionally, for water or oil-immersion lenses, vibration of the sample stage can cause disturbance or ripples in the immersion media that can lead to significant distortion in the images. A robust alternative to the use of mechanical scanning stages is a remote focusing system that allows both the objective and the sample to be stationary. One such solution is the employment of a tunable-focus liquid lens in conjunction with a microscope objective to achieve axial scanning through a sample being imaged. Our work demonstrates the implementation of a robust, cost-effective and energy-efficient axial tuning solution for 3D microscopy based on thermos-responsive hydrogel-based tunable liquid lenses.

1 Introduction

1.1 Microlenses and microcameras

With the ever increasing need for miniaturized electronics, the demand for micro-optics is also rising steadily. Micro-optics can be broadly defined as 'optical systems that are between a few micrometres and a millimetre in size' [1]. The main factors contributing to the importance of micro-optics is the ease of integration, small size, low cost and robustness. Today micro-optics have wide ranging applications from cellphone cameras, surveillance equipment, endoscopes to videoscopes. Micro-optics spans a wide variety of optical devices including lenses, optical switches, digital micromirror devices. The work presented here revolves around fabrication, design and development of optical systems using microlenses. Microlenses or millimeter/submillimeter scale lenses are widely used in a variety of applications including biomedical imaging, optical communication, cellphone cameras and digital projectors.p

A broad way to categorize lenses is based on the lens material used i.e. solid and liquid lenses; each of which can be further classified as fixed-focus or tunable lenses. Tunable lens can be defined as an optical device that can focus a light beam at different distances along the optical axis, by changing either the properties of the lens material or one of the geometric parameters. While fixed focus lenses have been in use for several years, tunable-focus optics are becoming increasingly popular in applications like surgical imaging, cameras.

On the one hand, new materials, such as liquids, distensible membranes, liquid crystals and deformable structures, may be used for the fabrication of tunable microlenses, and on the other, phenomena such as surface tension, pressure, mechanical deformation and the application of electric or magnetic fields may be employed to tune the optical characteristics. In this work, we

will mainly focus on tunable focus lenses formed by deformable liquid/liquid interfaces. Among these, liquid focus-tunable lenses have emerged as the winning candidate in the past decade. Liquid lens technology is a rapidly progressing field driven by the promise of low cost fabrication, faster response, fewer mechanical elements, versatility and ease of customization for different applications.

Previously our research group has focused on the development of technologies for fabrication and performance enhancement of focus-tunable liquid lenses. This work shifts the focus to leveraging these techniques to address some significant challenges in two biomedical imaging applications – laparoscopic imaging and 3D microscopy.

1.2 Laparoscopic imaging

Over the last decade, the field of minimally invasive surgeries (MIS) has evolved very rapidly. It was estimated in 2003 that over 2 million laparoscopic operations were performed in the United States [1] . Laparoscopy covers a wide range of surgical procedures from the more common such as appendectomy and inguinal hernia repair to more complex such as colorectal resections or fundoplication of the stomach for reflux disease. Laparoscopy is a minimally invasive surgical procedure in which operations are performed through small ‘keyhole’ incisions. The clinical benefits of MIS for patients are twofold – cosmetic and physical – reduction of disfigurement as well as pain and physiological responses to the stresses of open surgery [2-5].

The key elements in a basic diagnostic laparoscopic surgery are a light source, camera, surgical instruments, ‘trocars’ or surgical ports and a pneumoperitoneum (or gas-insufflation of the abdominal cavity). The abdominal cavity if first insufflated with carbon dioxide gas to elevate the abdominal wall above the internal organs and provide a safe working space. Trocars or surgical

ports are then inserted through small (typically 0.5 – 1.5 cm) incisions. A trocar functions as a portal for the subsequent introduction of surgical instruments, cameras and light sources into the surgical cavity. Current laparoscopic imaging technology relies on a single fixed-focus camera through one of the ports, thus facing five fundamental challenges – limited field of view (FoV), lack of depth perception, occupation of a dedicated port by the camera, need for extensive maneuvering of the camera during surgery by an assistant and glare from highly reflective organ surfaces [6].

A panoramic, 3-dimensional (3D) vision of the surgical field, closely resembling the view in a conventional open surgery, is highly desirable in laparoscopy. It helps expedite surgical tasks and enhances the safety of surgical procedures [7-8]. A clear field of view (FoV) is critical to allow identification of vital structures, manipulation of tissue, and optimal surgical performance in order to safely complete each operation. A single camera provides a small FoV and limited depth perception due to the flat, 2D view. Some commercial systems claim 3D vision by employing a pair of closely spaced cameras. However, the narrow baseline between the cameras and the resulting low disparity limit the accuracy of depth recovery. More importantly, a two-camera pair cannot provide sufficient viewing angles to ensure an unobstructed view of the surgical region despite the presence of surgical instruments.

In the past, research solutions have proposed using wedge prisms [9], panomorph lenses [10] and mirror attachments [11-12] to increase the FoV. Nonetheless, these methods suffer from a multitude of issues ranging from aberrations to blind zones. Other research solutions to address these challenges through software techniques for 3-D depth recovery have also had limited success [13].

Current laparoscopes demand one port exclusively for imaging rather than instrumentation. In addition, constant maneuvering of the camera between ports is required to adjust the viewing angle of the surgical field. Several groups have bypassed these requirements by means of imaging tools tethered [14], sutured [15] or magnetically anchored [16] to the abdominal wall. However, these invasive solutions result in additional puncture points or tugging of the abdominal wall, increasing the invasiveness of the laparoscopic procedures.

Other research alternatives such as single-port surgery allowing multiple ports and curved instruments via one site [17] suffer greatly from reduced freedom of movement of surgical instruments and challenging maneuvers, rendering them less practical. Current commercial robotic platforms such as the Da Vinci system [18] offer some advantageous solutions but at the price of very high cost and large footprints.

Existing imaging solutions only address the aforementioned challenges individually and offer partial benefits over the current technology, at best. We previously reported on a reconfigurable fixed-focus, micro-camera array with panoramic vision [19-21]. In our work, we present a new, comprehensive approach to addressing the aforementioned challenges in one system.

1.3 3D Microscopy

Conventional wide-field microscopy is one of the most widely used optical microscopy technique. This technique typically captures a two dimensional image of a specimen. For a volumetric visualization of the sample or to enable depth scanning along the axial direction, it is necessary to move the sample relative to the fixed focal plane of the microscope objective. For this purpose, a mechanical z-scanning stage is typically employed. The stage enables the focal plane

to move through the sample. Typical approaches used to achieve axial scanning are a motorized stepper stage or a piezoelectric stage. While stepper motors offer the advantage of unlimited travel distance, they suffer from hysteresis. Piezoelectric stages on the other hand, help eliminate hysteresis at the cost of the travel distance which is reduced to 100-200 μm. Both the types of stages, however, are bulky and cause vibrations and wobble in the sample due to high inertia [22]. Additional care is required to avoid mechanical overshoots and backlash from the tip touching the sample. Additionally, for water or oil-immersion lenses, vibration of the sample stage can cause disturbance or ripples in the immersion media that can lead to significant distortion in the images. A robust alternative to the use of mechanical scanning stages is a remote focusing system that allows both the objective and the sample to be stationary. One such solution is the employment of a tunable-focus liquid lens in conjunction with a microscope objective to achieve axial scanning through a sample being imaged. Our work demonstrates the implementation of a robust, cost-effective and energy-efficient axial tuning solution for 3D microscopy based on thermos-responsive hydrogel-based tunable liquid lenses.

References

[1] K.A. Cullen, M.J. Hall, and A. Golosinskiy "Ambulatory surgery in the United States," *Natl Health Stat Report*. Vol. 11, no. 11, pp. 1-25, 2009.

[2] A. Rané, Scar-less surgery. London: Springer, 2013.

[3] O. Aziz ,T. Athanasiou, P.P. Tekkis, S. Purkayastha, J. Haddow, V. Malinovski, P. Paraskeva, and A. Darzi, "Laparoscopic versus open appendectomy in children: a meta-analysis," *Ann Surg*. vol. 243, no. 1, pp. 17-27, 2006.

[4] F. Keus, J.A. de Jong, H.G. Goosze, and C.J. van Laarhoven, "Laparoscopic versus open cholecystectomy for patients with symptomatic cholecystolithiasis," *Cochrane Database Syst Rev.* vol. 4, no. 4, 2006.

[5] S. Sauerland, R. Lefering, and E.A. Neugebauer, "Laparoscopic versus open surgery for suspected appendicitis," *Cochrane Database Syst Rev*. , vol. 4, no.4, 2004.

[6] H. Xin, J.S. Zelek, and H. Carnahan, "Laparoscopic surgery, perceptual limitations and force: A review," *First Canadian Student Conference on Biomedical Computing*, Kingston, Ontario, Canada, vol. 144, 2006.

[7] Y. Naya, K. Nakamura, K. Araki, K. Kawamura, S. Kamijima, T. Imamoto, N. Nihei, H. Suzuki, T. Ichikawa, and T. Igarashi, "Usefulness of panoramic views for novice surgeons doing retroperitoneal laparoscopic nephrectomy," *Int. J. Urol.*, vol. 16, pp. 177-80, 2008.

[8] S.B. Bhayani and G.L. Andriole, "Three-Dimensional (3D) Vision: Does It Improve Laparoscopic Skills? An Assessment of a 3D Head-Mounted Visualization System," *Rev. Urol.,* vol. 7, no. 4, pp. 211-214, 2005.

[9] E. Kobayashi, K. Masamune, I. Sakuma, and T. Dohi, "A Wide-Angle View Endoscope System Using Wedge Prisms," *Medical Image Computing and Computer-Assisted Intervention*, Springer Berlin Heidelberg, 2000, pp. 661-668.

[10] P. Roulet, P. Konen, M. Villegas, S. Thibault and P. Garneau, "360° endoscopy using panomorph lens technology," *Proc. SPIE Endoscopic Microscopy*, vol. 7558, pp. 1-13, 2010.

[11] R. Sagawa, T. Sakai, T. Echig, K. Yagi, M. Shiba, K. Higuchi, T. Arakawa, and Y. Yagi, "Omnidirectional Vision Attachment for Medical Endoscopes," *Proc. the Eighth Workshop on Omnidirectional Vision, Camera Networks and Non-classical Cameras*, Marseille, France, 2008.

[12] Arber, R. Grinshpon, J. Pfeffer, L. Maor, S. Bar-meir and D. Rex, "Proof-of-concept study of the Aer-O-Scope omnidirectional colonoscopic viewing system in ex vivo and in vivo porcine models," *Endoscopy*. Vol. 39, no. 5, pp. 412-417, 2007.

[13] D. Stoyanov, A. Darzi, and G. Z. Yang, "A Practical Approach towards Accurate Dense 3D Depth Recovery for Robotic Laparoscopic Surgery", *Comput. Aided Surg*., vol. 10, pp. 199–208, 2005.

[14] C. A. Castro, A. Alqassis, S. Smith, T. Ketterl, S. Yu, S. Ross, A. Rosemurg, P. P. Savage, and R. D. Gitlin, "A Wireless Robot for Networked Laparoscopy," *IEEE Trans. on Biomed. Eng.,* vol. 60, pp. 930-936, 2013.

[15] H. Tie, P. K. Allen, T. Nadkarni, N. J. Hogle, and D. L. Fowler, "Insertable stereoscopic 3D surgical imaging device with pan and tilt," *IEEE Int. Conf. on Biomedical Robotics and Biomechatronics*, Scottsdale, pp. 311-316, 2008.

[16] S. L. Best, and J. A. Cadeddu, "Development of magnetic anchoring and guidance systems for minimally invasive surgery", *Indian J. Urol.*, vol. 26, pp. 418-422, 2010.

[17] L. Mereu, S. Angioni, G. B.Melis, and L. Mencaglia, "Single access laparoscopy for adnexal pathologies using a novel reusable port and curved instruments," *Int J Gynaecol Obstet.*, vol. 109, no. 1, pp. 78-80, 2010.

[18] M. Satava, J.C. Bowersox, Mack M, and T. M. Krummel, "Robotic surgery: state of the art and future trends," *Contemp Surg*., vol. 57, pp. 489–499, 2001.

[19] A. Kanhere, B. Aldalali, J. A. Greenberg, C. P. Heise, L. Zhang, and H. Jiang, "Reconfigurable Micro-Camera Array with Panoramic Vision for Surgical Imaging," *J. Microelectromech. Syst.*, vol. 22, no. 5, pp. 989-991, 2013.

[20] A. Kanhere, K. Van Grinsven, C.-C. Huang, Y.-S. Lu, J. Greenberg, C. Heise, Y. Hu and H. Jiang, "Multi-Camera Laparoscopic Imaging with Tunable Focusing Capability," *Solid-State Sensors, Actuators, and Microsystems Workshop*, Hilton Head Island, SC, June 8-12, 2014.

[21] B. Aldalali, J. Fernandes, Y. Almoallem, and H. Jiang, "Flexible Miniaturized Camera Array Inspired by Natural Visual Systems," *J. Microelectromech. Syst.*, vol. 22, no. 6, pp. 1254-1256, 2013.

[22] Y. Nakai, M. Ozeki, T. Hiraiwa, R. Tanimoto, A. Funahashi, N. Hiroi, A. Taniguchi, S. Nonaka, V. Boilot, R. Shrestha, J. Clark, N. Tamura, V. M. Draviam, and Hiromasa Oku, "High-speed microscopy with an electrically tunable lens to image the dynamics of in vivo molecular complexes," Review of Scientific Instruments, 86, 013707, 2015.

2 Fixed-focus microcameras for laparoscopy

2.1 Introduction

Microcameras are very critical components in laparoscopic and single port surgery [1]. Two of the important desired features in surgical imaging systems are panoramic vision and depth of field. Panoramic vision in these camera systems is very useful in increasing the field of view (FoV) for the surgeon [2]. Enhanced depth perception in surgical imaging systems is known to increase speed and precision in surgery [3][4]. The current approach for surgical imaging is to employ a single camera with a fisheye lens. However, a fisheye lens provides a hemispherical FoV at the expense of poor off-axis resolution and chromatic aberration [5]. Even in systems using two fisheye lenses for enhanced depth perception, the problem of reduced peripheral resolution persists. An alternative technique is to combine the images from multiple cameras with small lenses for added flexibility and redundancy without distortion. However, existing multi-camera systems are macroscale and hence unsuitable in the microscopic world, especially medical applications. We previously reported a concept of a multi camera system [6]. Here we report on a further miniaturized design with more detail and extended functionality in terms of the horizontal FoV, compared to a zero-degree laparoscopic camera. Our prototype consists of a micro panoramic vision system that includes four micro-cameras controlled simultaneously by mechanical umbrella rib-like actuators, offering reconfigurable angle of view and depth perception. This system is configured in the context of laparoscopic surgery and single-port surgery.

2.2 Mechanism

The concept of our work as indicated in Fig. 1 was designed for laparoscopy as a target application. In laparoscopy, an access port is used for insertion and maneuvering of instruments during surgery. Our design incorporates the imaging system on the periphery of such a port to ensure minimum interference with the surgical instruments.

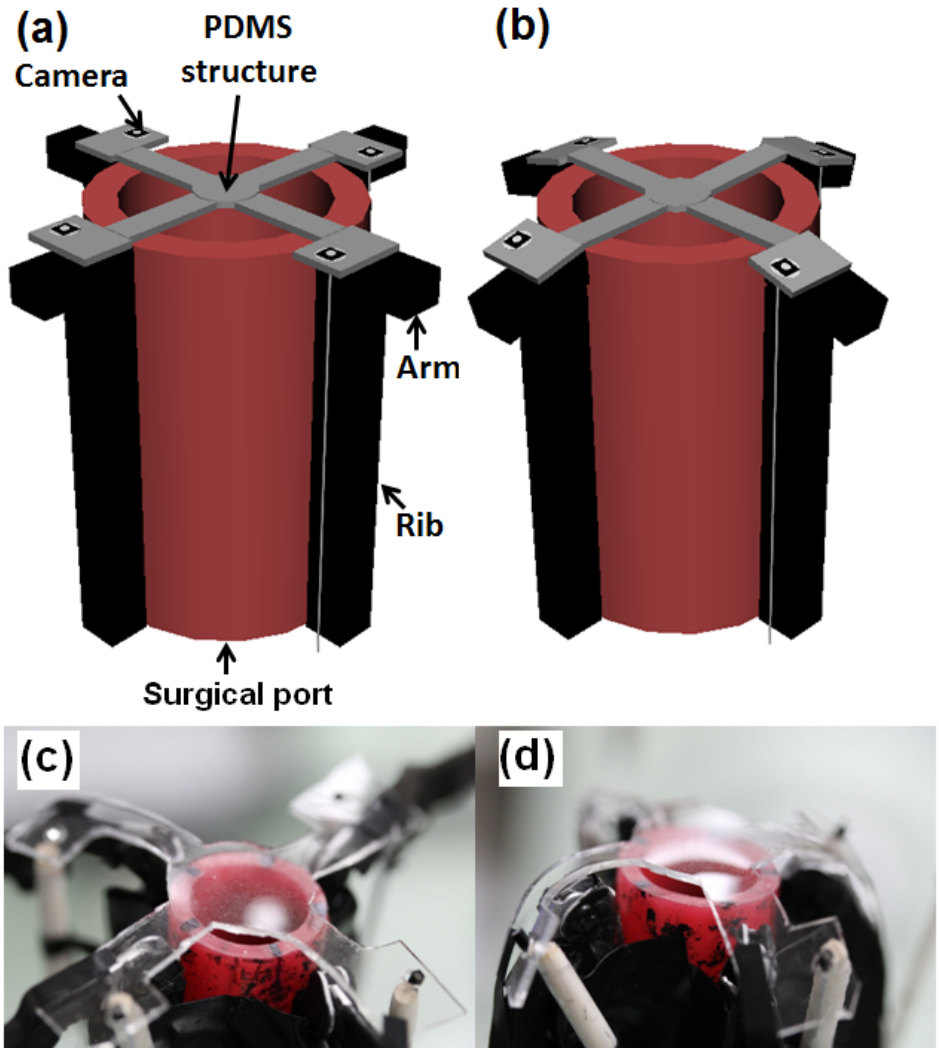

Figure 2.1. Prototype of the micro camera array. (a) and (b) are 3D schematics of two different configurations of the camera array while (c) and (d) are corresponding photo images of these two configurations of the four-camera imaging system around a surgical port.

Fig. 2.1(a)–(b) show 3-dimensional (3D) schematics of three representative configurations of the camera array, the transition between which can be achieved with mechanical actuators. The actuation was realized by using a network of four ribs each supporting one camera; the structure operates similar to an umbrella. The rib movement can be controlled simultaneously to orient the cameras at a desired angle. The goal of this design is to keep the device positioned closely around a laparoscopic port during insertion into the body. During surgical operation, the surgeon can flare out the array so that the cameras are oriented at desired angles, for an extended FoV.

By simultaneously changing the orientation of the four cameras, we can obtain variations in the viewing perspectives, depth of field and horizontal FoV. Dynamic stitching of panoramic views from multiple configurations can aid in a much greater horizontal FoV and depth, as compared to any of the individual configuration alone. For example, images from configurations in Fig. 2.1(a) [and (c)] and Fig. 2.1(b) [and (d)] together increase the horizontal FoV by approximately 85º and yield an increased depth of field as compared to Fig. 2.1(a) [and (c)] or Fig. 2.1(b) [and (d)] alone. A real time video display of composite of scenes from different configurations can greatly enhance the view of the surgical field.

2.3 Fabrication

The key to the success of coordinated functioning of the camera array is precision in symmetric positioning (and repositioning) of a camera with respect to the laparoscopy port and the other cameras, to achieve maximum horizontal FoV. To this end, we fabricated a polydimethylsiloxane (PDMS) structure to maintain the alignment of the four cameras.

Fig. 2.1 (c)-(d) show the micro-camera array. It includes four 1mm × 1mm NanEye cameras (AWAIBA Lda, Madeira, Portugal) integrated with convex lenses (focal length, f = 5.0 mm) and

connected together by a PDMS structure. The PDMS structure comprises of a circular center with four bridges radially pointing outward with one camera holder at the end of each bridge. The center of the PDMS structure is pinned to the laparoscopy port. This ensures that when the mechanical arms supporting the four cameras move simultaneously, the relative positions of the cameras with respect to the port and each other remain unchanged. As shown in Fig. 1, the PDMS bridges flex or stretch when the orientation angle of the cameras is changed, to keep their alignment intact. Batch production of all the PDMS camera holders and interconnecting bridges was possible using the process shown in Fig. 2.2.

Fig. 2.2 shows the fabrication process of the PDMS bridges and lens holders. A 350μm-thick chamber was first filled with a photopatternable prepolymer isobornyl acrylate (IBA), made as per the recipe found in [7,8]. The prepolymer IBA was then exposed under ultraviolet light at 8.3 mW/cm^2 for 26 seconds using a photomask to define the mold for the bridges and lens holders. Uncured PDMS was then poured over the poly-IBA mold and cured for 4 hours at 80ºC to yield the final PDMS structure.

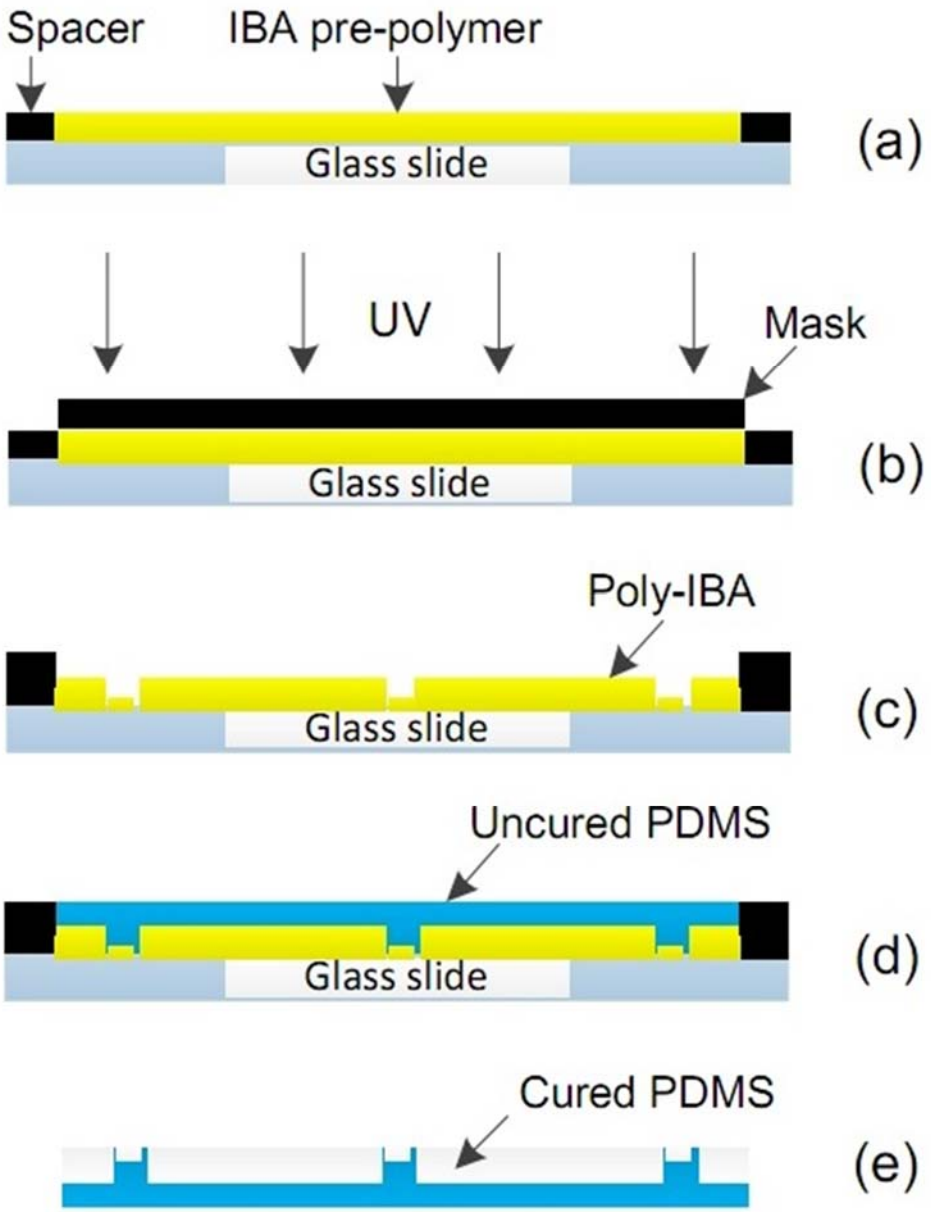

Figure 2.2 Batch fabrication process for all PDMS camera holders and bridges. This framework is critical for alignment of the four cameras symmetrically around the laparoscopy port and with each other. (a) Spacers on a glass slide are used to define thickness of poly-IBA structure. (b) Mask with spacers form a cavity filled with IBA. UV exposure is used to cure the IBA pre-polymer. (c) Poly-IBA mold for bridges and lens holders is formed. (d) Uncured PDMS is poured onto the poly-IBA mold and cured for 4 hours at 80oC. (e) Final PDMS camera holders and bridge structure.

2.4 Experimental results

The experimental setup as demonstrated in Fig. 2.1 was achieved by symmetric placement of the mechanical actuators and the cameras around the port. Motion of the four arms supporting the cameras was controlled simultaneously by umbrella rib-like actuation. Images from the four cameras were obtained for different configurations. Panoramic views for each configuration were obtained by stitching the four images. The test scene comprised of 17 dice, labeled with letters, forming a cross. The center of the laparoscopy port was placed perpendicular to the center of the central dice labeled 'A', at a distance of 8 cm away from the top of the dice for all the experiments.

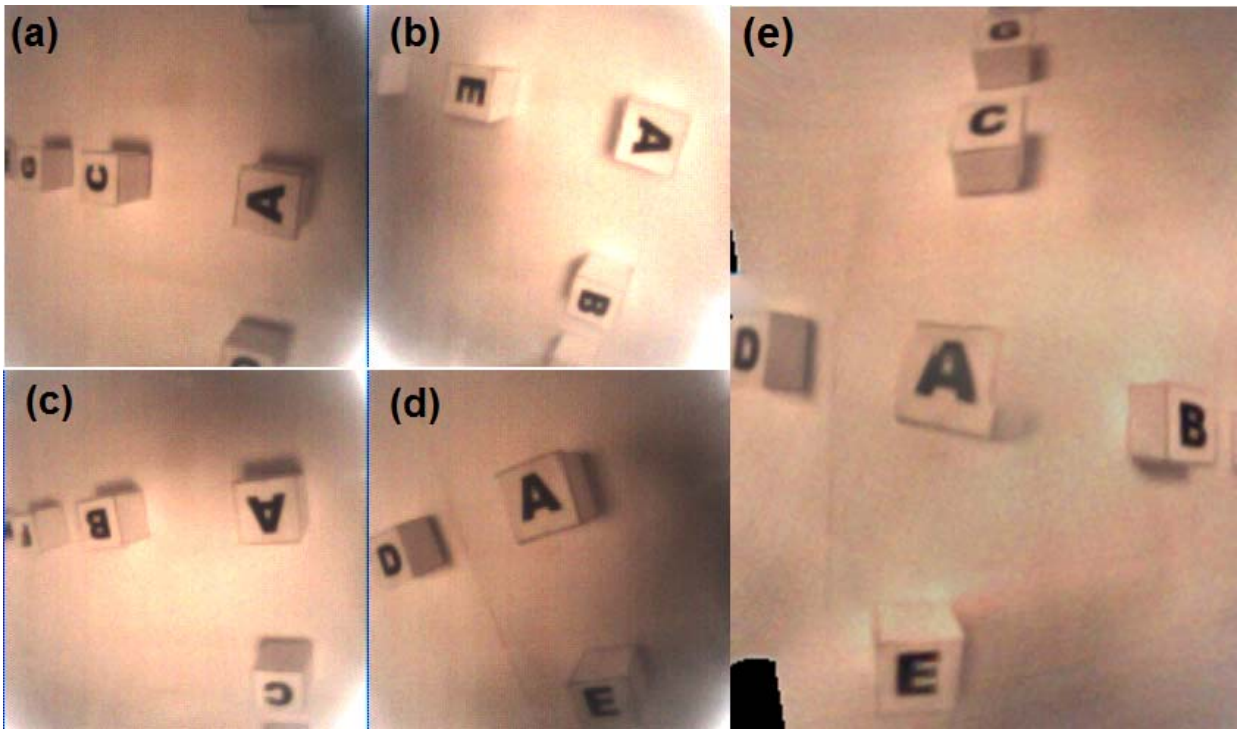

Figure 2.3(a) – (d) Individual images captured by the four cameras placed in a configuration shown in Fig. 1(a) and (c). (e) The panorama obtained by stitching (a) - (d).

Fig. 2.3 shows a dataset of images obtained from configuration shown in Fig. 2.1(a) and (c) as well as a panoramic image combined from those four images. The images were combined using a commercial software, PTgui™. The resulting image lends an extended FoV with no visible seams. The achieved horizontal FoV is 45º. In all our experiments, since the scene is much far away relative to the distance between the cameras, the FoV can be approximated as the total sum of FoV of individual cameras minus the overlapping FoV between cameras. The resulting panorama shows a slight distortion that is not seen in the individual images due to limitations of the commercial stitching software.

The critical requirement for obtaining a meaningful panorama from any configuration of the camera array is that the four individual images should have a sufficient overlap with each other so as to enable the stitching operation. The simultaneous actuation of the mechanical arms along with the camera alignment achieved with the PDMS holders ensures precision of the orientation angle of each arm within +/- 5 degrees of the desired angle. Fig. 2.4 shows another dataset of images for the same scene, captured with a different camera configuration shown in Fig. 2.1(b) and (d).

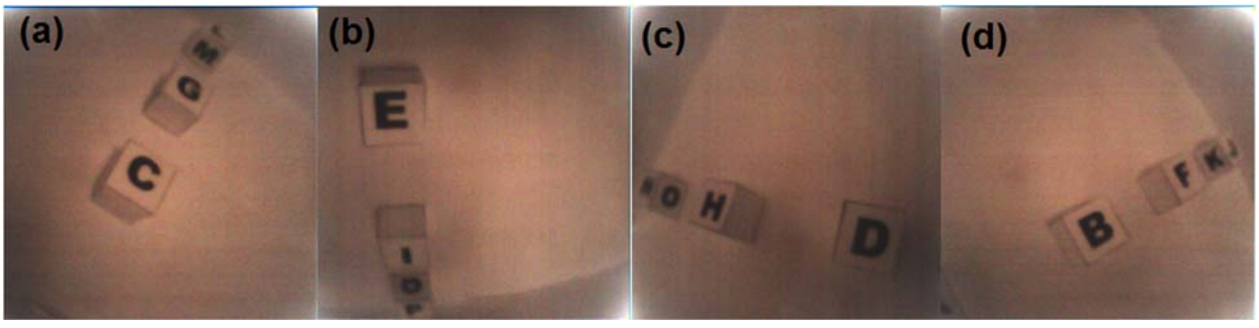

Figure 2.4(a) – (d) Individual images captured by the four cameras configured as shown in Fig. 1(b) and (d).

Images from different configurations contain information of the same scene from distinct viewing perspectives. Hence stitching of images from two different configurations would result in an image with a greater horizontal FoV and a better depth of field. Fig. 2.5(a) demonstrates such a composite image obtained by stitching images in Fig. 2.5(a) – (d) and Fig. 2.4(a) – (d). The horizontal FoV increases from 45º in Fig. 2.3(e) to 130º in Fig. 5(a).

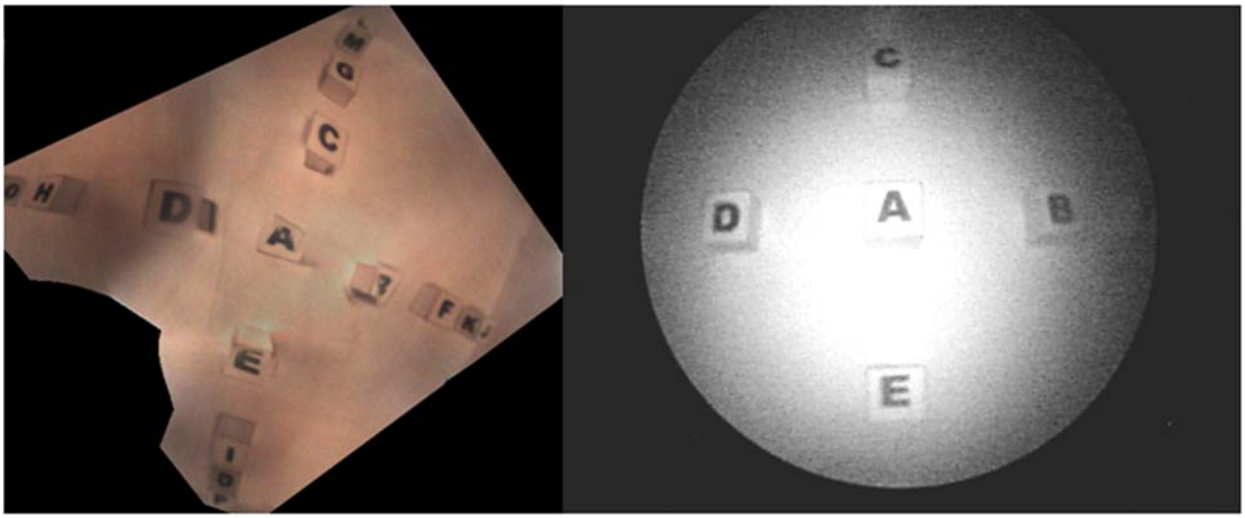

Figure 2.5. (a) Composite image obtained by stitching images from Fig. 3(a) - (d) and Fig. 4(a) - (d). (b) Image obtained by a 5mm zero-degree laparoscopic camera with same experimental parameters. Significant increase in the FoV is achieved in (a) as compared to (b).

To compare our images with existing laparoscopic imaging, we repeated our experiment with a commercial 5mm zero-degree laparoscopic camera (Stryker, Kalamazoo, MI, USA). The laparoscopic camera was also placed 8 cm away, perpendicular to the center of the dice labeled 'A'. The acquired image, as shown in Fig. 2.5(b), clearly shows that the current laparoscopic imaging system suffers from lower resolution, smaller FoV and aberrations near the edges. The panorama obtained from configuration shown in Fig. 2.1(a) and (c) has a FoV comparable to the image in Fig. 2.5(b). However, as seen from Fig. 2.5(a), stitching of panoramas from multiple configurations significantly increases FoV, compared to a laparoscopic camera.

Conclusion

We demonstrated an experimental prototype of a multi-camera micro panoramic vision system. The device uses mechanical arms as actuators to provide reconfigurable angles and positions of the cameras with respect to a laparoscopic surgical port. Our prototype yields a significantly larger FoV as compared to a commercial laparoscopic camera. Future work includes higher-level integration of the flexible structures, image sensors, optical components, all connectors and cables, and further miniaturization of the whole system. Our ultimate goal is to realize a spherical vision system with capabilities for real-time tracking of surgical instruments as well as 3D rendition of the surgical scene. Minor modifications in the arrangement of the cameras can make the system applicable in other non-surgical applications where the maneuvering space is limited.

References

[1] R. R. Ivatury, L. F. Zantut, J. A. Yelon, "Laparoscopy in the new century," *Surgical Clinics of North America*, vol. 79, no. 6, pp. 1291-1295, 1999.

[2] M. O. Schurr, G. Buess, W. Kunert, E. Flemming, H. Hermeking, L. Gumb, "Human sense of vision: A guide to future endoscopic imaging systems," *Minimally Invasive Therapy & Allied Technologies*, vol. 5, no. 5, pp. 410-418, 1996.

[3] H. Xin , J. S. Zelek and H. Carnahan, "Laparoscopic surgery, perceptual limitations and force: A review," *Proceedings of the First Canadian Student Conference on Biomedical Computing,* Kingston, Ontario, Canada, 2006, pp. 44-46.

[4] S.H. Kong, B.M. Oh, H. Yoon , H.S. Ahn, H.J. Lee, S.G. Chung, N. Shiraishi, S. Kitano, H.K.Yang, "Comparison of two- and three-dimensional camera systems in laparoscopic performance: a novel 3D system with one camera," *Surgical Endoscopy*, vol. 24, no. 5, pp.1132-1143, 2010.

[5] J.J. Kumler and M.L. Bauer, "Fisheye lens designs and their relative performance," *Proc. SPIE,* vol. 4093, San Diego, CA, 2000, pp. 360-369.

[6] A. Kanhere, B. Aldalali, L. Zhang, and H. Jiang, "Reconfigurable, Panoramic Vision Micro Camera Array," *IEEE Optical MEMS and Nanophotonics*, Banff, Canada, 2012, pp. 9-10.

[7] A. K. Agarwal, S. S. Sridharamurthy, D. J. Beebe, and H. Jiang, "Programmable autonomous micromixers and micropumps," *IEEE/ASME Journal of Microelectromechanical Systems*, vol. 14, no. 6, pp. 1409-1412, 2005.

[8] A.K. Agarwal, D.J. Beebe and H. Jiang, “Integration of polymer and metal microstructures using liquid-phase photopolymerization,” *Journal of Micromechanics and Microengineering*, vol. 16, pp. 332-340, 2006.

3 Thermo-responsive tunable-focus liquid lenses

3.1 Introduction

The term ‘liquid lenses’ refers to lenses formed with liquid/liquid or air/liquid or solid membrane/liquid interface, the shape of which can be controlled by numerous actuation mechanisms. Liquid lenses are rapidly emerging as promising replacements for solid microlenses in applications including photography [1], optical data storage [2], biomedical applications devices [3,4] and lab-on-a-chip devices [5,6]. They offer a unique advantage of ease of tunability of the focal length. The two basic strategies to achieve tunability are controlling the refractive index of the lens liquid and controlling the lens shape [7].

Liquid lenses can be tuned by modulating the refractive index of its liquid. Some of the common techniques used to change the refractive index include pressure control, electrowetting control, optical control, magnetic control, thermo-optic control, and electro-optic control. A change in liquid composition can also be achieved by mechanical pumping and mixing methods. Shape (and hence the focal length) of lenses formed by liquid/liquid interface or polymer membrane/liquid interface can be controlled by mechanical pressure [8,9], electromagnetic field [10], displacement [11], electrowetting [12-14] or dielectrophoretic effect [15,16].

However, all these types of tunable microlenses require external electric, pressure or magnetic controls. As a result, the optical system becomes bulky making it challenging to integrate the tunable microlenses with other optical components. In addition, it is highly undesirable to use high voltage or pressure in surgical imaging or other biomedical applications.

Our group previously reported on a unique hydrogel-based actuation technique for tuning the focal length of liquid lenses [17], which requires easy, inexpensive fabrication and eliminates

the need for bulky power sources for actuation. The key element of the design is a stimuli responsive hydrogel which functions as an actuator that can be used to induce a pressure to control the lens shape. The actuation mechanism can be temperature [18, 19], pH [20] or infrared [21]. The liquid lens is formed by an interface between water and oil. The lens liquid, water, is contained within structures made from the stimuli-responsive hydrogel and works as the lens liquid. In response to the corresponding environmental stimulus, the hydrogel structures reversibly contract or expand to absorb or release water, thereby changing the volume of the lens liquid and hence the shape of the lens interface. Here, a liquid tunable-focus microlens actuated by a temperature-responsive hydrogel is presented.

3.2 Principle of operation

The principle of operation of the thermo-responsive hydrogel tunable lenses is represented in the schematic shown in Fig. 3.1. The design consists of a thermal stimuli-responsive hydrogel ring placed within a microfluidic chamber filled with water. This chamber is sealed with an aperture slip with a circular opening centered over the ring. An oil chamber is then placed on top of the aperture slip. The opening in the aperture slip acts as the lens aperture. The water-oil meniscus is pinned along the lens aperture by surface treating the layers to create a hydrophobic-hydrophilic contact boundary. The initial meniscus, and thus the focal length, is determined by the volume of water filled in the water chamber. When the temperature of the lens structure is increased, the hydrogel ring responds by contracting due to the release of water via the hydrogel network interstitials. This results in a net change in the volume of the water located in the center of the ring. Since the aperture rim of the lens is pinned, this translates to an increase in the radius of curvature and a decrease in the focal length. This process is reversible with little hysteresis [19], which means that a decrease in temperature will cause the focal length to increase.

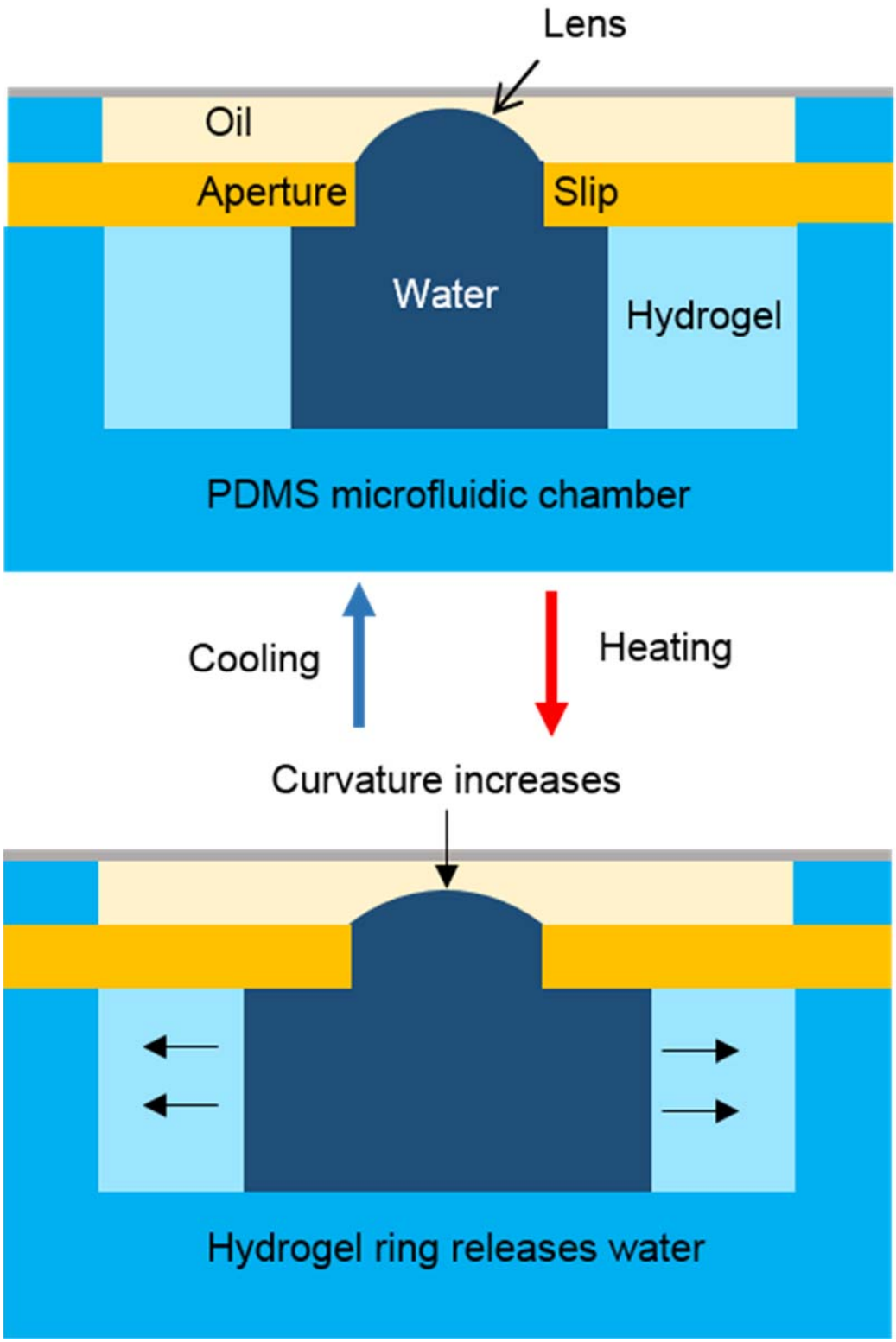

Figure 3.1 Schematic representation illustrating the operation of a thermo-responsive tunable liquid lens. As the local temperature increases, the hydrogel releases water and contracts, thereby increasing the radius of curvature and decreasing the focal length of the water-oil lens. This focal length change is reversible.

3.3 Design Considerations

The design of the hydrogel based tunable liquid lens is dominated by the desired geometry of the liquid-liquid interface. Since the aperture of the lenses is 1mm in diameter, the surface tension forces are stronger than gravitational forces and hence a spherical water-oil interface has been assumed. To calculate the minimum heights of water and oil containers, it is necessary to calculate the extent of protrusion of the lens interface into each of the containers. The following schematic illustrates the geometry of the lens structure.

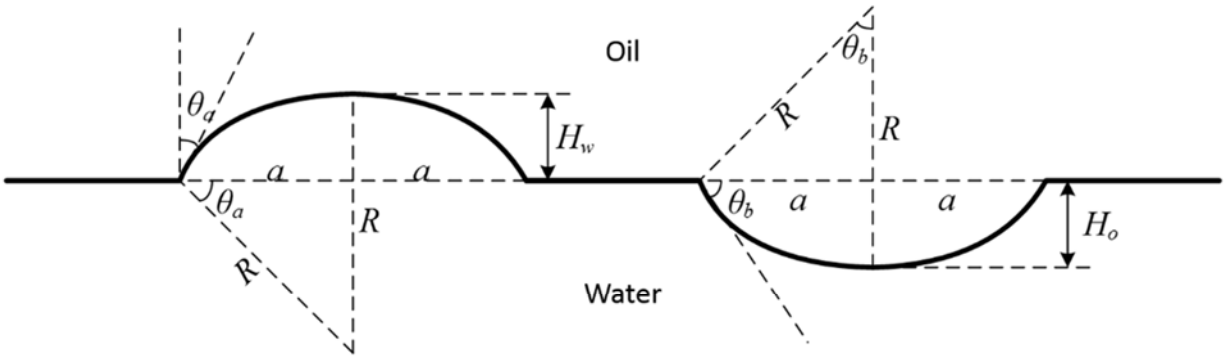

$$H_W = \frac{a}{\cos\theta_a}\left(1-\sin\theta_a\right) \qquad H_o = \frac{a}{\sin\theta_b}\left(1-\cos\theta_b\right)$$

$$\theta_a = 30^\circ \qquad \theta_b = 105^\circ$$

Figure 3.2 Schematic of side profiles of concave and convex states of water-oil lens. When the water profile bulges out into the oil container, the water-oil lens becomes divergent. The minimum height of the oil container is determined by the maximum height of the protrusion of the lens into the container. Similarly, when the water-oil meniscus curves into the water container, the water-oil lens becomes convergent. The minimum height of the water container is therefore determined by the maximum dip of lens into the water container.

The second important factor to be considered in tunable lens design is the focal length. Laparoscopic surgeries are most commonly performed within the abdominal cavity. Typically, a laparoscopic imaging system should be capable of viewing small features at the far end of the

surgical cavity as well as the larger protrusions, closer to the port. Hence we designed our liquid lenses with capability to tune within a wide range of 5 mm to 50 mm. The two main factors determining the focal length range of our tunable lenses are the lens aperture diameter and the actuation temperature. The lens aperture diameter of 1 mm was constrained by the smallest available commercial image sensor – 1 mm×1 mm NanEye cameras (AWAIBA Lda, Madeira, Portugal). The constraint on the temperature is placed by the higher temperature resistance limit of our commercial image sensor (T_{max} = 90°C).

3.4 Materials and fabrication techniques

3.4.1 Liquid-phase photopolymerisation

The main fabrication technique used to define multiple layers of the tunable lens structure is liquid-phase photopolymerization (LP3) followed by soft lithography. Microstructures are first patterned using LP3, then they are used to make lens molds in PDMS.

LP3 is an easy and low-cost method for fabrication of microstructures [22, 23]. In this method, a photopatternable liquid polymer that behaves like a liquid photoresist is used for rapid prototyping of microstructures in-situ under ultraviolet (UV) exposure. Unlike conventional lithography, LP3 does not require the spinning or casting of photosensitive materials, making it easier to mold multi-layer or high aspect ratio structures. Since the photosensitive material is a liquid, there is also an added advantage of self-planarization regardless of the topography of the underlying substrate.

The photosensitive polymer used pattern multiple layers of the lens structure is prepared by mixing the monomer—isobornyl acrylate (IBA, Surface Specialties UCB, Smyma, GA, USA), crosslinker— tetraethylene glycol dimethacrylate (TeGDMA, SigmaAldrich, St Louis, MO, USA)

and photoinitiator—2,2- dimethoxy-2-phenylacetophenone (DMPA, Sigma-Aldrich, St Louis, MO, USA) in the weight ratio 31.66:1.66:1.0. The three materials are mixed together in a glass vial using a sonicator. The polymer mixture functions like a negative-tone photoresist. Exposure to a UV light source (365 nm) causes the pre-polymer solution to harden (poly(IBA)). Photolithography was performed using an EXFO Acticure 4000 (EXFO Photonic Solutions, Inc., Mississauga, Ontario, Canada) UV light source (365 nm). High resolution (3600 dpi) film photomasks (Silverline Studio, Madison, WI, USA) are used to transfer patterns to the photosensitive polymer.

3.4.2 Thermo-responsive hydrogel - NIPAAm

A hydrogel is a three-dimensional network of polymer chains swollen within a solvent [24]. Hydrogels closely resemble natural rubber in high deformability and reversibility. Swelling or aggregation of the polymer chains can be triggered by various environmental conditions like temperature, pH and infrared light. Fig.3.3 illustrates a typical volume change of thermo-responsive hydrogel with respect to stimuli [24]. In this work, a type of thermo-responsive hydrogel, N-isopropylacrylamide (NIPAAm), was used as the actuator of the microlens. In this report, a type of thermo-responsive hydrogel, N-isopropylacrylamide (NIPAAm), is used as the actuator of the microlens.

NIPAAm exhibits a reversible volumetric change in response to the local temperature. At low temperatures, the hydrogel absorbs water causing a volume expansion; while at high temperatures it releases water and shrink in volume. NIPAAm hydrogel pre-polymer solutions consist of five components [18]: 0.545 g NIPAAm as the monomer, 0.0385 g 2,2-dimethoxy-2-phenylacetophenone (DMPA) as the co-monomer, 0.031 g *N*,*N*'-methylenebisacrylamide (NMBA) as the

cross-linker, 0.75 mL dimethyl sulfoxide (DMSO) and 0.25 mL gold deionized water as the solvents.

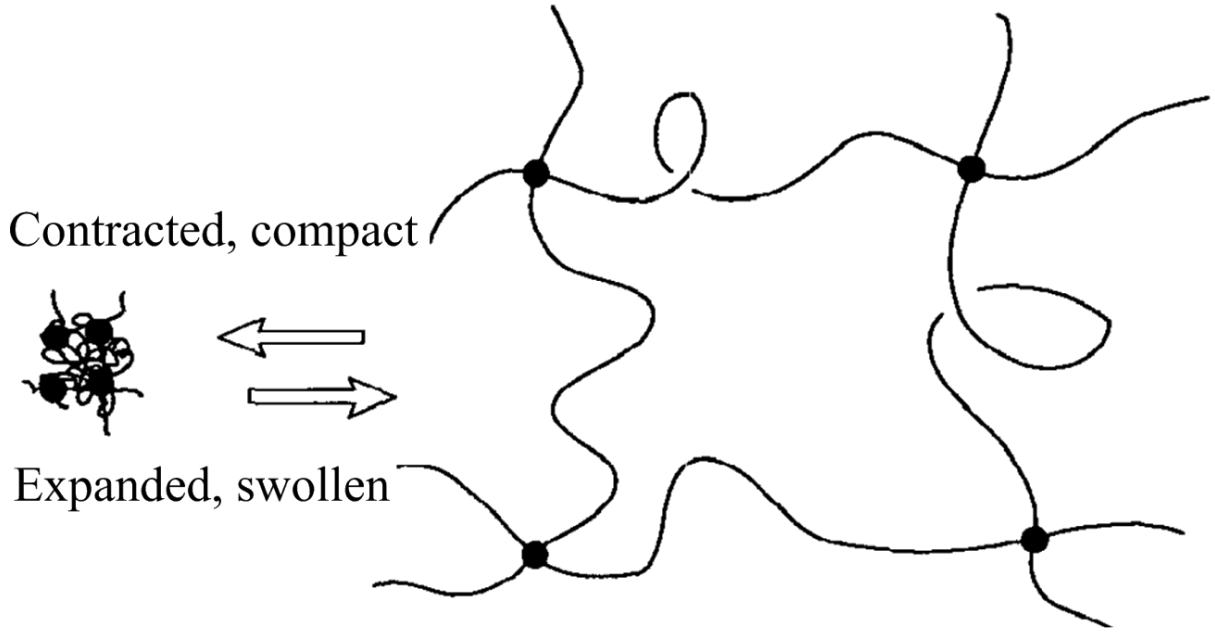

Figure 3.3 Hydrogel is cross-linked polymer chain attracted with external stimuli. It undergoes reversible volumetric transitions in response to changes in external environmental [24].

An important design consideration during fabrication of tunable lenses is the Lower Solution Critical Temperature (LCST) of the hydrogel. The LCST is the temperature point where a sharp phase transition occurs in the hydrogel. When heated to temperature above the LCST, the hydrogel responds by rapidly releasing water or contracting, thus reducing the focal length. When the temperature changes from above the LCST to below the LCST, the hydrogel volume changes by a factor of 10 [25]. During a surgery, it is undesirable to have an uncontrolled change in the focal length of a camera. Normal human body temperature is about 37ºC. If the LCST of the hydrogel is close to 37ºC, the focal length of the lens will change in response to body heat. To avoid this, we set the LCST of the hydrogel at 42ºC, to account for the deviations in body temperatures of patients.

3.5 Fabrication

The tunable lenses were fabricated using liquid-phase photopolymerisation (LP3). The thermo-responsive hydrogel, N-isopropylacrylamide (NIPAAm) was used to actuate the tunable lenses. The intrinsic LCST of NIPAAm is 32^0C. It was adjusted to 42^0C by incorporating 0.15 percent by volume of an ionizable monomer, 3-(methacryloylamino) propyl trimethylammonium chloride (MAPTAC), into NIPAAm.

A 300 μm thick cavity was defined on a glass substrate using double-sided adhesive spacers. This cavity was filled with a poly(isobornyl acrylate) (IBA) prepolymer mixture. Poly-IBA posts defining the water container (Ø=2.5 mm) were photopatterned through a photomask aligned on top of the cavity under UV radiance (8.0 mW cm^{-2} for 75 s). The chamber was then rinsed with ethanol to remove the unexposed solution. Another 200 μm thick chamber was created on top of this structure to define the base of the water container. Prior to transferring the pattern onto PDMS, octadecyltrichlorosilane (OTS) solution was vapor deposited onto polyIBA structure to render it hydrophobic. This surface treatment makes it easier to peel PDMS off the polyIBA mold. Then the chamber was filled with pre-cured polydimethylsiloxane (PDMS) and cured at 70°C for 4 hours before being peeled off the poly-IBA mold.

The sidewalls and the base of the PDMS water containers were treated with corona discharge plasma to render them hydrophilic. The water containers were subsequently filled with the NIPAAm (with added MAPTAC) hydrogel pre-polymer solution and then were photopatterned under UV radiance (I = 15 mW cm−2; t = 18 s) to form hydrogel rings in the containers.

Similar procedures were carried out to form a 250 μm thick PDMS with 1 mm circular openings defining the lens aperture. The side walls and the bottom surface of the aperture slip were

made hydrophilic with corona discharge treatment. The top surface of the aperture slip was left untreated and hence retained the natural hydrophobic nature of PDMS. This enables the formation of a pinning boundary for the water-oil lens.

Another 250 μm thick PDMS layer with a 2.5 mm aperture was bonded on top of the aperture slip to form the oil container. The containers were filled with deionized water and silicon oil consecutively, forming the immiscible water–oil interfaces for the microlenses. The lens was sealed with a glass cover slip. The cross section of this fabrication process is shown in Fig. 3.4.

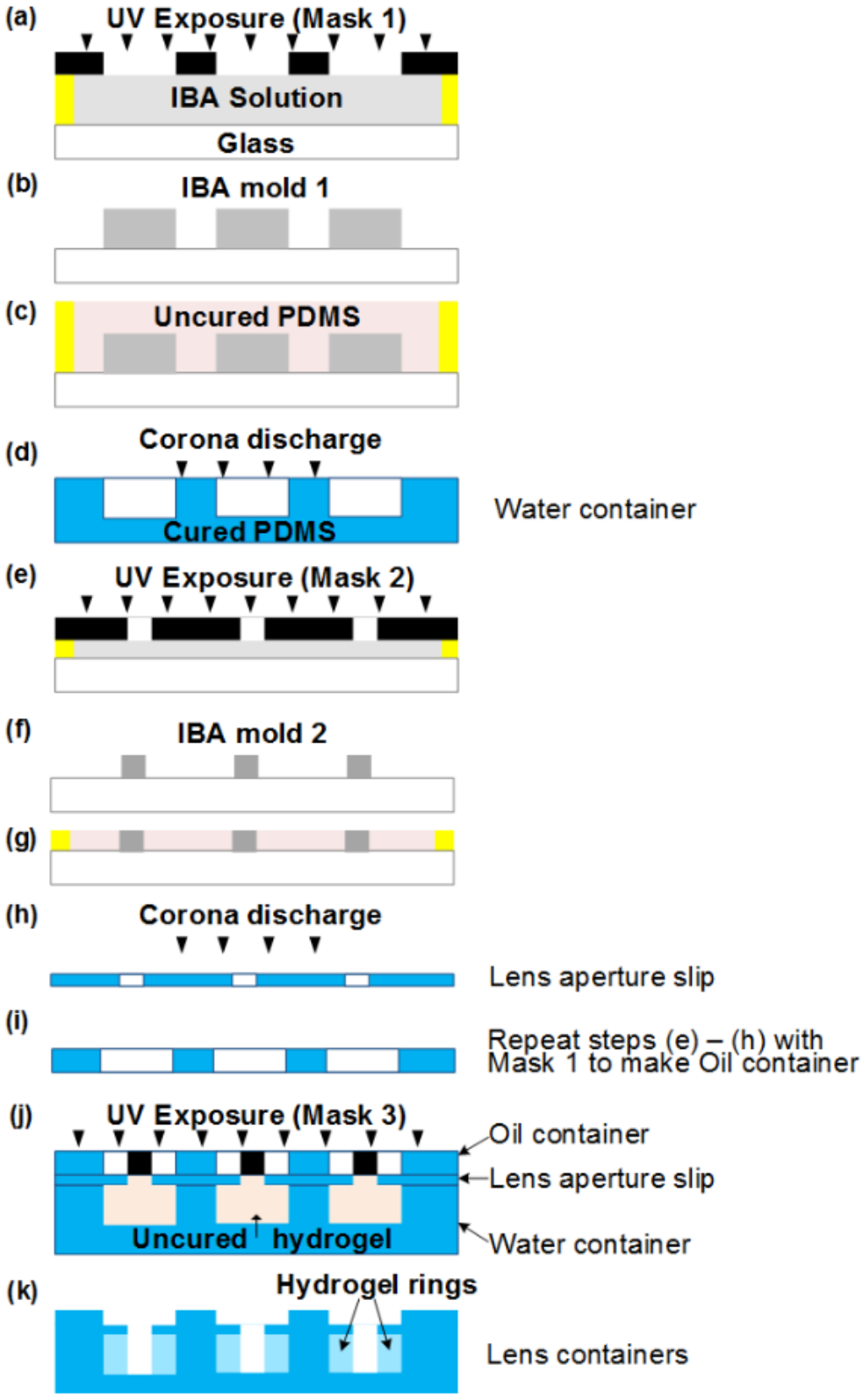

Figure 3.4 Fabrication process flow for thermo-responsive hydrogel based tunable liquid lenses

3.6 Characterization

3.6.1 Focal Length measurements

For identical temperatures, the focal length range of microlenses varies with the initial volume of water filled in the water containers. To analyze these variations, three sets of microlenses were fabricated with initial water volumes of 1.25 μL, 1.5 μL, and 1.7 μL. Within each set were five microlenses with the same initial water volume. The focal lengths of these microlenses were measured by computing the distance at which a collimated laser light passing through the microlens can be focused onto an optical screen. Fig. 3.5 shows a plot of the focal lengths versus temperature, averaged for each water volume. The average response time to tune a lens between the two extremes of its focal length range was ~20 seconds. Across the temperature range of 42^0C to 70^0C, an initial water volume of 1.5 μL yields a focal length range suitable for our application. For all the subsequent experiments, the initial water volume filled in the microlenses was 1.5 μL. However, even with the same initial water volume, the focal length of different lenses at the same temperatures varies within an error margin of 10%. This is due to the variations in the temperature-dependent volume change of hydrogel rings.

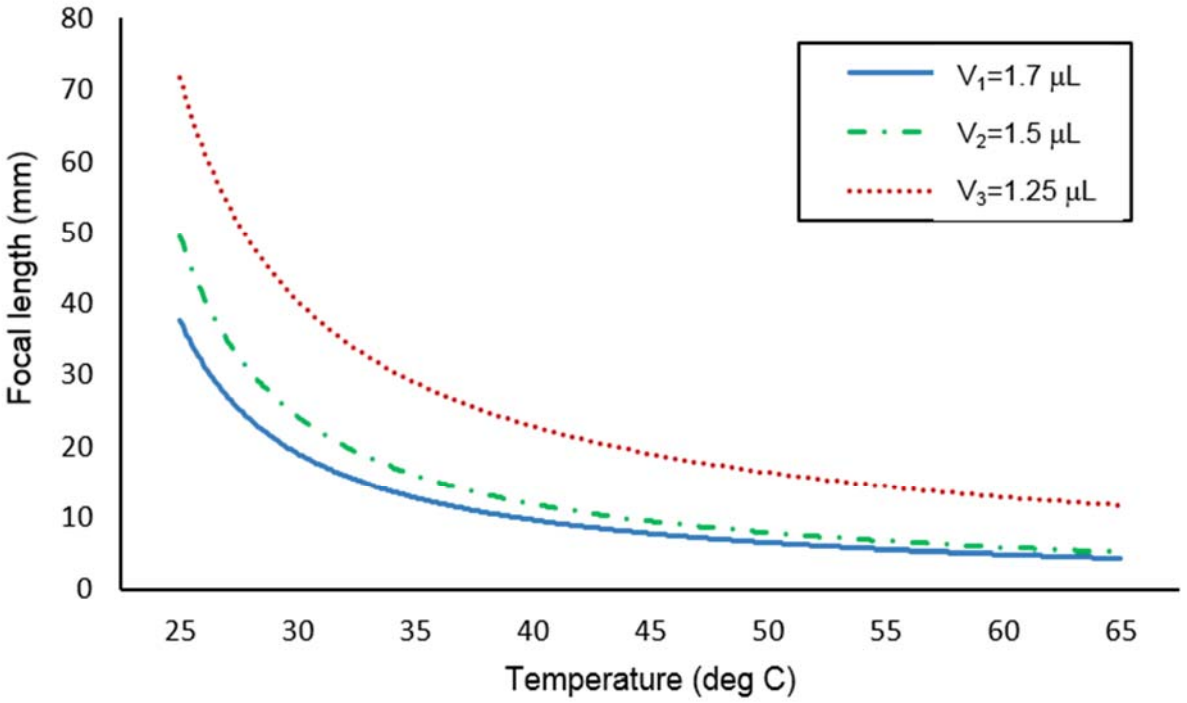

Figure 3.5 Focal lengths of microlenses plotted against temperatures for initial water volumes of 1.25 µL, 1.5 µL, and 1.7 µL filled in the liquid lenses. 1.5 µL water containers yielded an optimum focal length range when the temperature was varied from 42^0C to 75^0C.

3.6.2 Imaging performance

The resolving power of the lens was measured by imaging a 1951 USAF resolution test chart. Fig. 3.6 shows the image obtained by a microlens tuned to a focal length of 20 mm. The smallest resolvable features were 10.10 line pairs per mm. The lens design was simulated using the sequential ray tracing mode of a commercial light-ray tracing software, ZEMAX (ZEMAX Development Corporation, Bellevue, WA, USA). The pinned water-oil interface was assumed to be spherical since the two liquids have comparable densities [13]. Point spread function (PSF) analysis was performed to yield normalized light intensities at three different focal lengths.

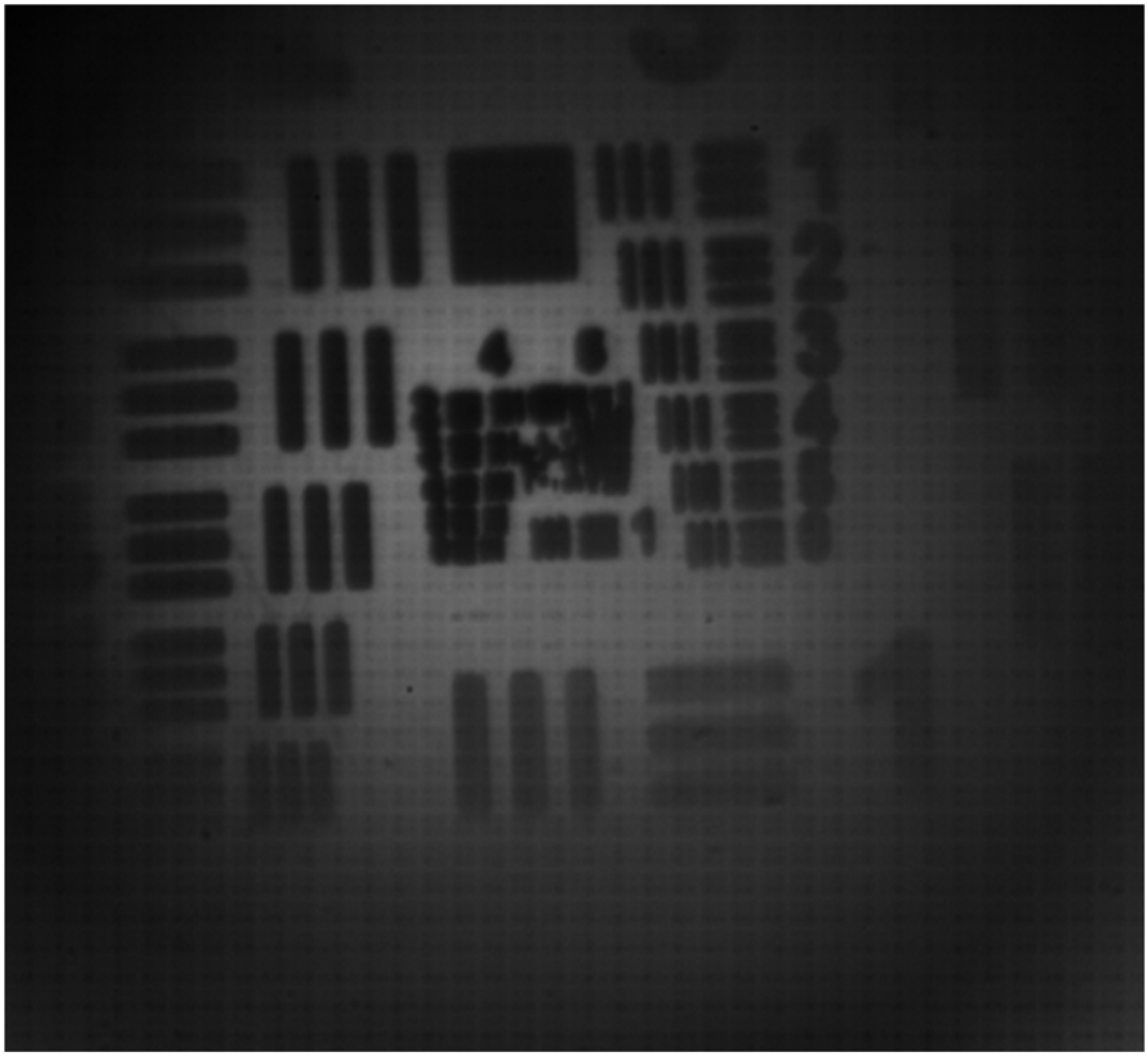

Figure 3.6 Image of the 1951 USAF resolution target as seen by a microlens with a focal length of 20 mm. The smallest resolvable features are element 3 in group 3 corresponding to a resolution of 10.10 line pairs/mm.

Spherical aberrations at these focal lengths were then calculated as the full width at half maximum of the PSF [21], as shown in Fig. 3.7. The normalized light intensity profiles at different focal lengths, and the corresponding spherical aberrations were also measured experimentally. A collimated laser source (632 nm) was used to illuminate a tunable microlens from the bottom. The image of the focused laser spot was recorded using a CCD camera (BCN-C050-U, Mightex Systems, Toronto, ON, Canada). As the focal length of the lens was tuned, the camera was moved

along the optical axis and positioned at the focal point. Normalized light intensities were extracted from these images at three different focal lengths and the corresponding spherical aberrations were calculated. Fig. 3.7. shows that the experimental and simulation results for spherical lens aberrations are in agreement within a reasonable margin of error.

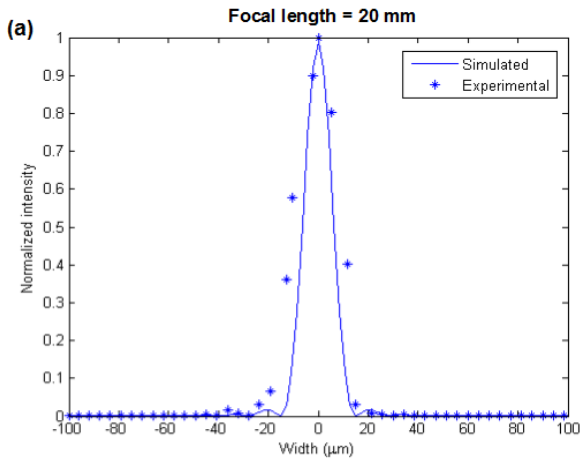

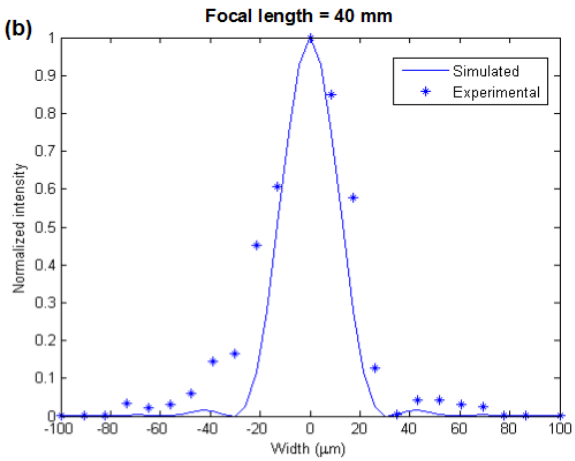

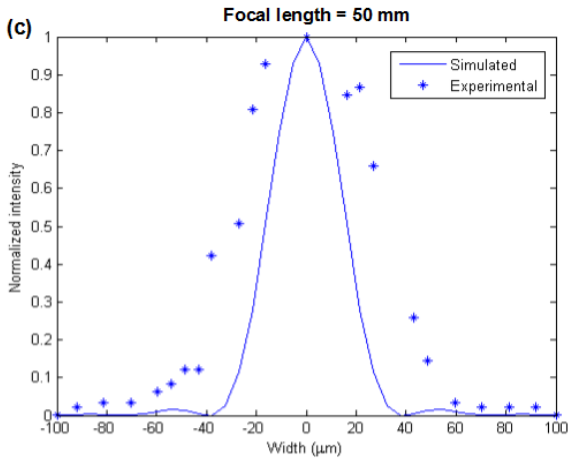

Focal length (f)	Spherical aberration (μm)	
	Simulated values	Experimental values
20 mm	12.48 μm	16.05 μm
40 mm	25.92 μm	42.96 μm
50 mm	32.44 μm	67.86 μm

Figure 3.7 Simulated and experimental normalized light intensity profiles obtained by imaging a laser beam focused by microlenses at focal lengths (a) 20 mm (b) 40 mm and (c) 50 mm. The corresponding spherical aberration values shown in the table are calculated as the full width at half maximum.

References

[1] S. Kuiper and B.H.W. Hendriks, "Variable-focus liquid lens for miniature cameras," *Appl. Phys. Lett*., 85, 1128 (2004).

[2] B.H.W. Hendriks, S. Kuiper, M.A.J. Van As, C.A. Renders, and T.W. Tukker, "Electrowetting-based variable-focus lens for miniature systems," *Opt. Rev.,*12, 3, 255–259, 2005.

[3] B.A. Flusberg, E.D. Cocker, W. Piyawattanametha, J.C. Jung, E.L.M. Cheung, and M.J. Schnitzer, "Fiber-optic fluorescence imaging," Nat. Methods, 2, 941–950, 2005.

[4] A. Divetia, Tsung-Hsi Hsieh, Jun Zhang, Zhongping Chen, Mark Bachman, and Guann-Pyng Li, "Dynamically focused optical coherence tomography for endoscopic applications," Appl. Phys. Lett., 86, 103902, 2005.

[5] J.C. Roulet, R. Völkel, H.P. Herzig, E. Verpoorte, N.F. de Rooij, and R. Dändliker, "Microlens systems for fluorescence detection in chemical microsystems," Opt. Eng., 40, 814–821, 2001.

[6] Jeonggi Seo and Luke P. Lee, "Disposable integrated microfluidics with self-aligned planar microlenses," Sens. Actuators B Chem., 99 (2–3), 615–622, 2004.

[7] Nguyen, Nam-Trung, "Micro-optofluidic Lenses: A review", *Biomicrofluidics*, 4, 031501 2010.

[8] K. H. Jeong, G. L. Liu, N. Chronis et al., "Tunable microdoublet lens array," *Optics Express*, vol. 12, no. 11, pp. 2494-2500, 2004.

[9] D. Y. Zhang, V. Lien, Y. Berdichevsky et al., "Fluidic adaptive lens with high focal length tunability," *Applied Physics Letters*, vol. 82, no. 19, pp. 3171-3172, 2003.

[10] S.W. Lee, and S. S. Lee, “Focal tunable liquid lens integrated with an electromagnetic actuator,” *Applied Physics Letters*, vol. 90, no. 12, pp. 121129, 2007.

[11] H. Ren and S. T. Wu, “Variable-focus liquid lens by changing aperture,” *Appl. Phys. Lett.*, vol. 86, no. 21, pp. 211107–211107, 2005.

[12] B. Berge and J. Peseux, "Variable focal lens controlled by an external voltage: An application of electrowetting," *The European Physical Journal E*, vol. 3, no. 2, 159-163, 2000.

[13] S. Kuiper, and B. H. W. Hendriks, “Variable-focus liquid lens for miniature cameras,” *Applied Physics Letters*, vol. 85, no. 7, pp. 1128-1130, 2004.

[14] T. Krupenkin, S. Yang, and P. Mach, “Tunable liquid microlens,” *Appl. Phys. Lett.*, vol. 82, pp. 316, 2003.

[15] C. C. Cheng, and J. A. Yeh, “Dielectrically actuated liquid lens,” *Optics Express*, vol. 15, no. 12, pp. 7140-7145, 2007.

[16] H. Ren, and S. T. Wu, “Tunable-focus liquid microlens array using dielectrophoretic effect,” *Optics Express*, vol. 16, no. 4, pp. 2646-2652, 2008.

[17] L. Dong, A. K. Agarwal, D. J. Beebe and H. Jiang, “Adaptive liquid microlenses activated by stimuli-responsive hydrogels,” *Nature*, vol. 442, pp. 551-554, 2006.

[18] L. Dong, A.K. Agarwal, D. J. Beebe, and H. Jiang, “Variable-focus liquid microlenses and microlens arrays actuated by thermoresponsive hydrogels,” *Advanced Materials*, vol. 19, no. 3, 401-405, 2007.

[19] X. Zeng, C. Li, D. Zhu, H. Cho, and H. Jiang, "Tunable microlens arrays actuated by various thermo-responsive hydrogel structures,"*IOP Journal of Micromechanics and Microengineering*, vol. 20, 115035, 2010.

[20] L. Dong and H. Jiang, “pH-adaptive microlenses using pinned liquid-liquid interfaces actuated by ph-responsive hydrogel,” Applied Physics Letters, vol. 89, no. 21, 211120, 2006.

[21] X. Zeng and H. Jiang, “Tunable liquid microlens actuated by infrared light-responsive hydrogel,” Applied Physics Letters, vol. 93, 151101, 2008.

[22] D. J. Beebe, J. S. Moore, Q. Yu, R. H. Liu, M. L. Kraft, B. H. Jo, and C. Devadoss, "Microfluidic tectonics: A comprehensive construction platform for microfluidic systems," Proceedings of the National Academy of Sciences of the United States of America, vol. 97, pp. 13488-13493, 2000.

[23] A. K. Agarwal, S. S. Sridharamurthy, D. J. Beebe, and H. R. Jiang, "Programmable autonomous micromixers and micropumps," Journal of Microelectromechanical Systems, vol. 14, pp. 1409-1421, 2005.

[24] Y. Li and T. Tanaka, "Phase-Transitions of Gels," *Annual Review of Materials Science,* vol. 22, pp. 243-277, 1992.

[25] J. Wang, Z. Chen, M. Mauk, K-S. Hong, M. Li, S. Yang, and H. Bau, "Self-Actuated, Thermo-Responsive Hydrogel Valves for Lab on a Chip," *Biomed. Microdevices*, vol. 7, no. 4, pp. no. 313-322, 2005.

4 Tunable-focusing laparoscopic camera

Laparoscopy is a minimally invasive surgical procedure. In the past two decades, it has gained tremendous popularity. In the United States alone, no less than 2-3 million laparoscopic surgeries are performed every year [1]. This figure shows the key elements in a basic diagnostic laparoscopic surgery - a light source, camera, surgical instruments, 'trocars' or surgical ports and a pneumoperitoneum (or gas-insufflation of the abdominal cavity). The abdominal cavity is first insufflated with carbon dioxide gas to elevate the abdominal wall above the internal organs and provide a safe working space. The surgeon then makes multiple incisions ~0.5 – 1.5cm in size. Trocars or surgical ports are then inserted through these incisions. A trocar functions as a portal for the subsequent introduction of surgical instruments, cameras and light sources into the surgical cavity.

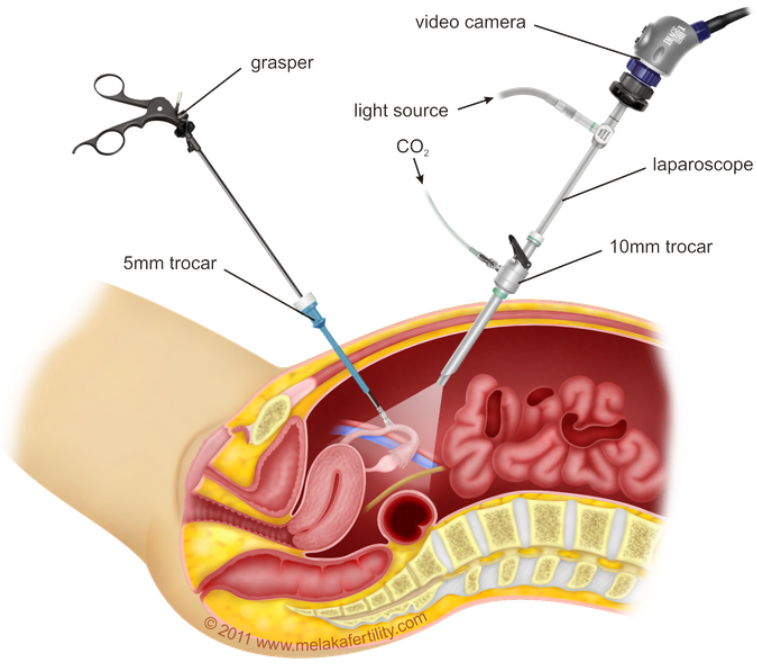

Figure 4.1. An overview of the key elements of a laparoscopic surgery [2]

Our system features an integrated trocar-camera assembly (TCA) and a user interface with image acquisition, illumination and optical tuning controls. Our unique approach enables easy adaptability of the system for both single-port and multi-port laparoscopies without compromise on any of the design benefits. Fig. 4.2 shows a schematic of our system, as implemented for multi-port laparoscopy.

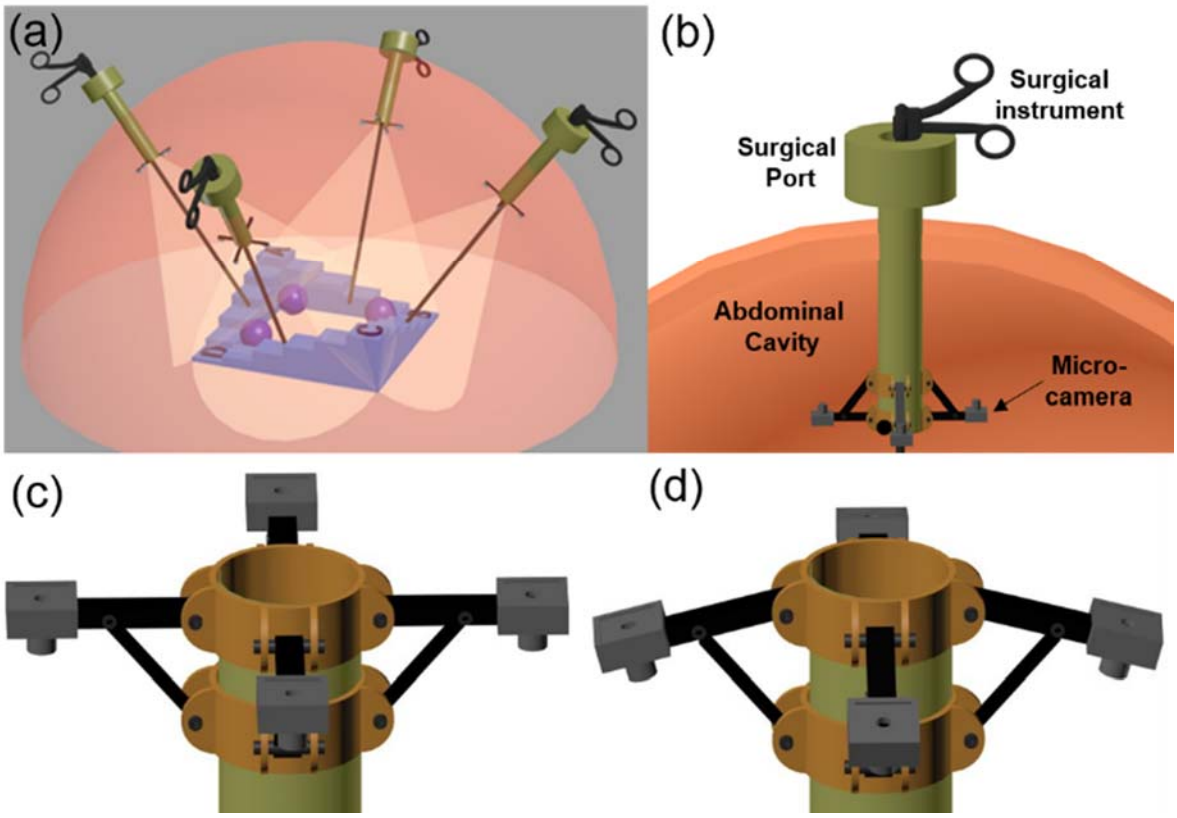

Figure 4.2 Schematic representation of (a) our system, as implemented in a multi-port laparoscopic surgery. (b) The cross-sectional view of an integrated trocar-camera assembly after insertion within an abdominal cavity. (c)-(d) The reconfigurability of camera perspectives using an umbrella-like mechanical actuator.

A hemispherical dome structure is used to illustrate an abdominal, surgical cavity with four incision points or ports. During a laparoscopic procedure, the four TCAs will first be inserted into the surgical cavity, one through each incision (port). Each TCA features an array of four tunable micro-cameras. The TCAs will then be positioned to view the surgical region of interest from four

viewing perspectives in such a manner, that most of the scene elements are visible to more than one TCA. The redundancy arising due to such an imaging strategy ensures that every detail in the scene will be captured by at least one port. This feature is critical for viewing smaller elements occluded from view by surgical instruments, shadows or larger elements.

Following this, the images from individual cameras in each TCA will be displayed with focus settings, as controlled by the surgeon and these images can further be combined and processed at his/her wish. There will be no further human intervention required throughout the surgery to move, remove or replace the cameras. The trocar will remain accessible for surgical instruments. The surgeon can acquire images, control the illumination intensity and control the focus of each camera through a user interface panel.

The TCA integrates an array of four microcamera units with a surgical port so that multiple cameras may be deployed into the abdominal cavity through an incision, without any additional surgical operation. In addition, it is affixed to the distal end of the port to capture images, while reconfiguring viewing perspectives through simple mechanical actuation. In our current prototype, the design of the TCA is preliminary, the focus being primarily on assembly and integration of the microcamera units.

The TCA consists of four microcameras assembled symmetrically around the trocar, connected together by a mechanical assembly. The mechanical design of the assembly is similar to an umbrella frame. As shown in Fig. 4.2(c), the assembly consists of four mechanical arms, each supporting one tunable microcamera. The arms are interconnected via a mechanical assembly that enables opening and closing of the arms, similar to the spokes of an umbrella.

The frame is mounted along the periphery of the distal end of a surgical port, thereby keeping the port accessible. This ensures that the imaging system never interferes with the instruments in the port. The design of the actuation frame enables the reconfiguration of the cameras to ensure complete coverage of the surgical scene without the need for constant maneuvering during surgery.

Images acquired from individual cameras in any one frame position will present distinct yet overlapping viewing perspectives of the same scene. Hence they can be stitched seamlessly for a much wider FoV in the resulting panoramic image. The use of multiple cameras allows for large FoV with reduced aberration (e.g. compared with fisheye-lens) while the optical tunability of the microcameras significantly improves the quality and depth perception of the image. In this chapter, we discuss our work on development of the multi-camera laparoscopic system. As shown in Fig. 4.3, each camera module of the Trocar camera assembly consists of four components – an image sensor, a thermo-responsive tunable lens and an integrated heater-sensor actuator for optical tuning and a polarizer for glare reduction.

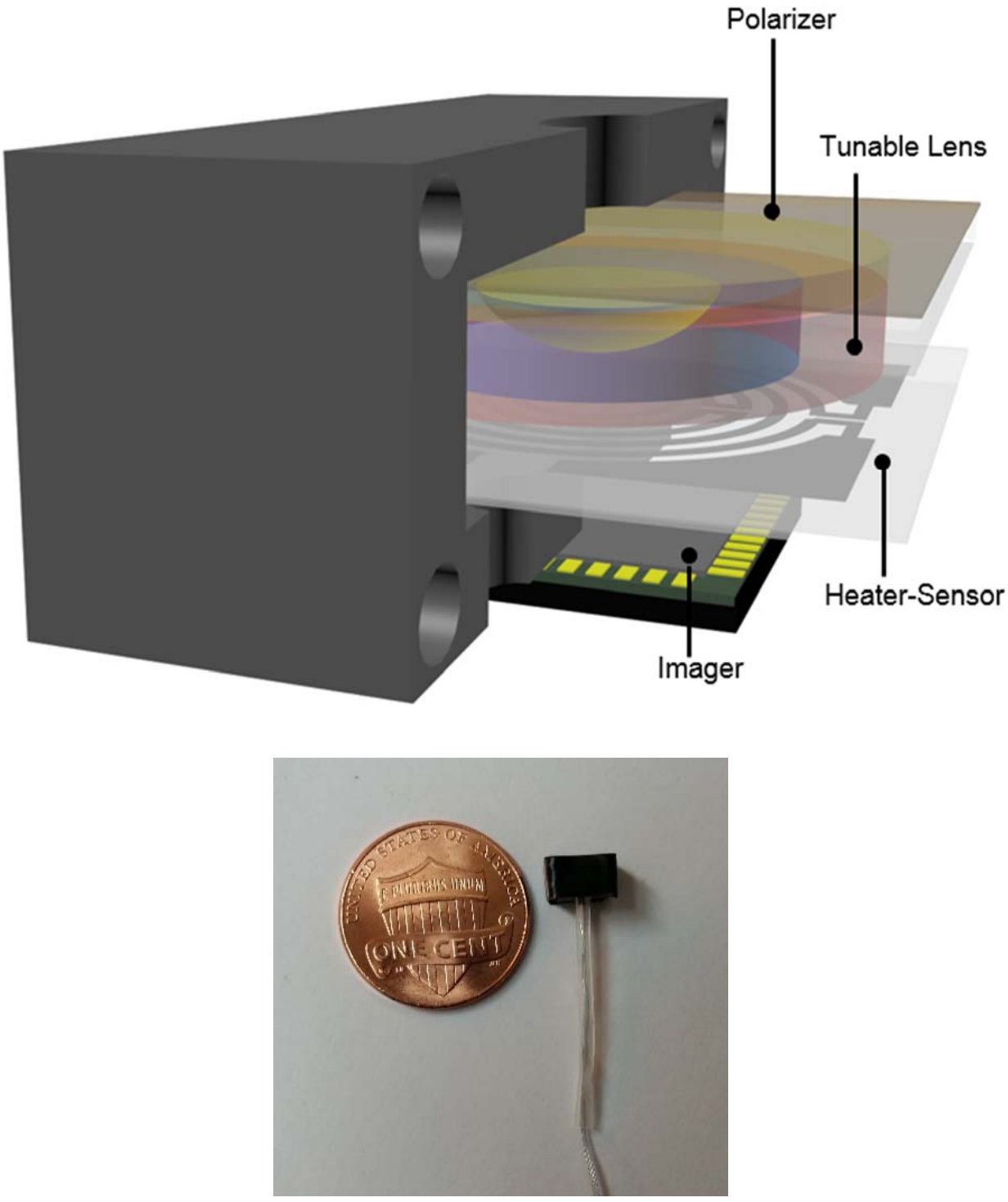

Figure 4.3 (Top) A three dimensional representation of the assembly of a microcamera unit. Every camera module comprises of a commercial image sensor (1 mm × 1 mm) , a tunable thermo-responsive liquid lens with an integrated heater-sensor and a polarizer. (Bottom) An image of one microcamera shown for scale next to a US penny.

4.1 Design considerations

The factors influencing our choice of the microheater were (1) form factor suitable for easy integration with lenses, (2) uniformity of heat distribution, (3) ease of heat dissipation after operation and (4) preventing thermal shock to the image sensor. We chose a coil type resistive heater design, as shown in Fig. 4.4 for easy alignment with the hydrogel ring structure. The coil design also minimizes hotspots due to absence of sharp corners [3].

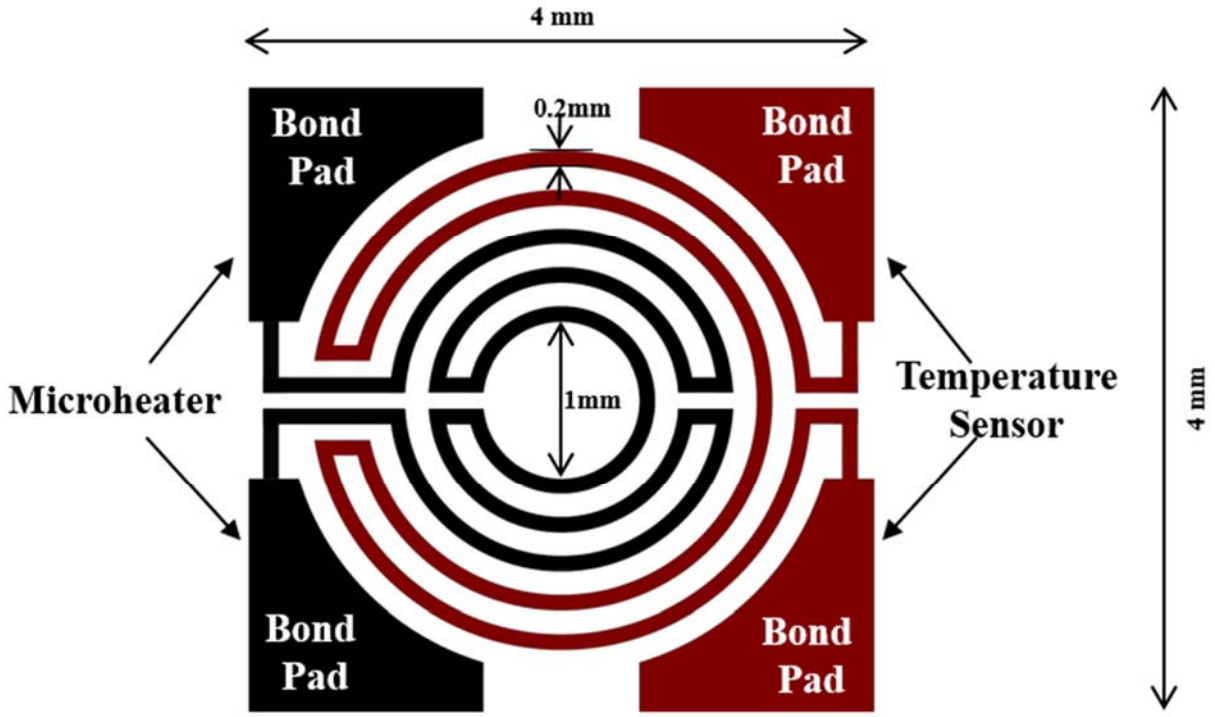

Figure 4.4 Schematic of the integrated microheater-sensor design. The coil track shown in black is the microheater; whereas the coil shown in red the temperature sensor. The width of the coil track is 0.2 mm whereas its thickness is 200 nm.

Ideally the change in the focal length of the microlens should closely track the actuation temperature of the microheater. To this end, we chose the coil type design of the microheater to align directly under the hydrogel ring pattern. In addition, the microheater was encapsulated inside the sensor coil, so as to ensure accurate sensing and feedback control. The heating material should

be made of a material with a high thermal conductivity to ensure a short response time. We chose aluminum (Al) as the heater material for ease of fabrication.

Since the microheater is resistive, its resistance will change with temperature and can be calculated from the equation

$$R_t = R(1 + \alpha T)$$

R_t – Resistance at temperature, T

R – Resistance at ambient temperature, 25 °C

α – Temperature coefficient of resistance (0.00429 for Al at 25 °C)

Resistance of the microheater at ambient temperature of 25 °C can be calculated from the equation

$$R = \frac{\rho L}{wt}$$

ρ – Resistivity (2.82 x 10^{-8} Ω-m for Al at 25 °C)

L – Length of heater

w – width of heater

t – thickness of heater

For our microheater dimensions (L=28.634 mm; w=0.1 mm; t=250 nm), its resistance at room temperature is 32.29 Ω.

4.2 Fabrication

Thermal actuation and tuning of the lens was achieved with a microheater placed at the base of the lens, fabricated as shown in Fig. 4.5 using lift-off process. The microheater was fabricated on a PDMS substrate to maintain biocompatibility, flexibility and easy integration with the tunable lens. A layer of PDMS was first spun onto a photoresist coated glass slide and cured at 70^0C for 4 hours. Subsequently, a 2 μm thick layer of Parylene-C was deposited onto the PDMS layer, to improve the adhesion of metal onto PDMS. A 250 nm thick Al layer was then sputtered onto this layer followed by photolithography and wet etching (H_3PO_4:HNO_3:CH_3COOH:H_2O in ratio 3:3:1:1 at 40 ^{0}C for 75 s) to define the microheater coil.

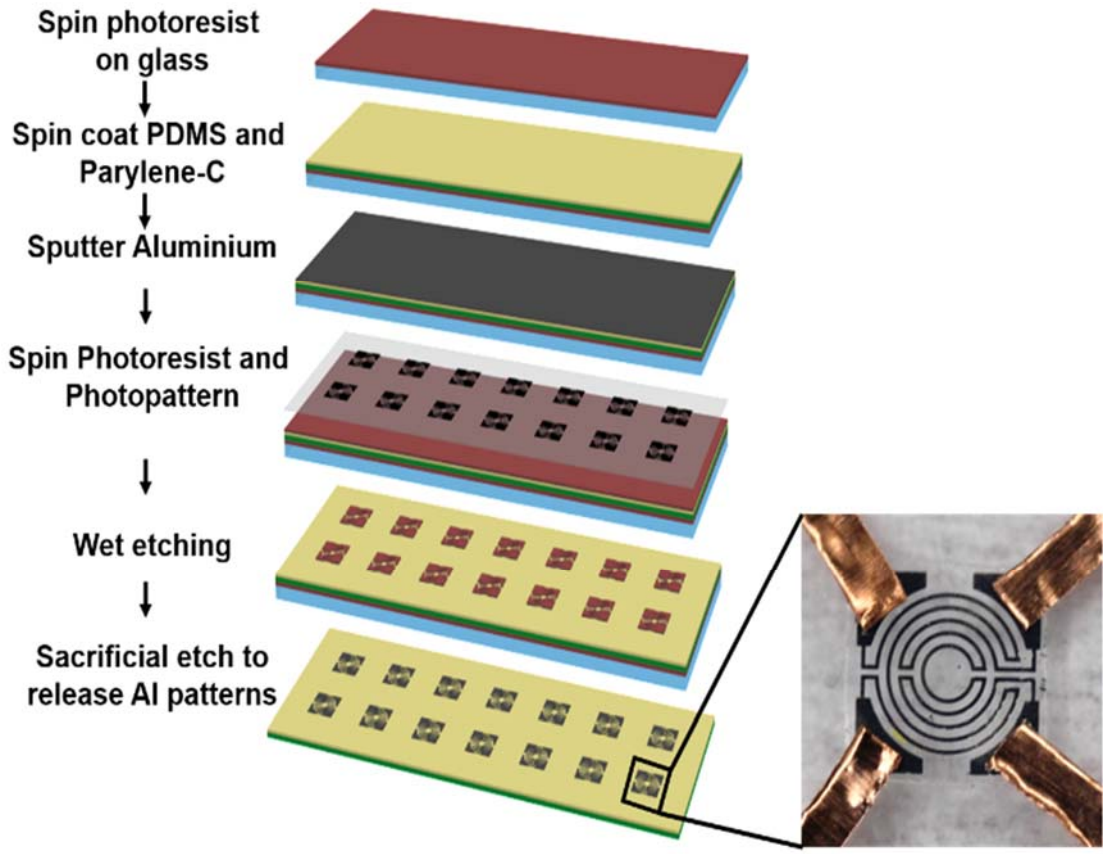

Figure 4.5 Fabrication process flow for aluminum micro heater coil patterned on PDMS using lift-off process

4.3 Simulation and Characterization

The thermal behavior of the microheater design was analyzed using ANSYS simulation software (ANSYS, Inc.). The heat dissipation from the heater to the surrounding air ($T=25^0C$) was assumed to be through convection. The steady state thermal-electric analysis module of ANSYS was employed to simulate the temperature distribution in the heater. The results in Fig. 4.6 show that the heat distribution is localized within the heating element. Also, the temperature towards the edges of the device is much lower. This is crucial in our design to avoid over-heating of the surrounding tissue, since this could pose a high risk during surgery [4]. Within the active heater region, temperature uniformity is obtained within a reasonable tolerance 6.66%. The results in Fig. 4.6 were simulated at a time step of t = 1s, indicating a very rapid ramp up to the desired temperature in the heating element.

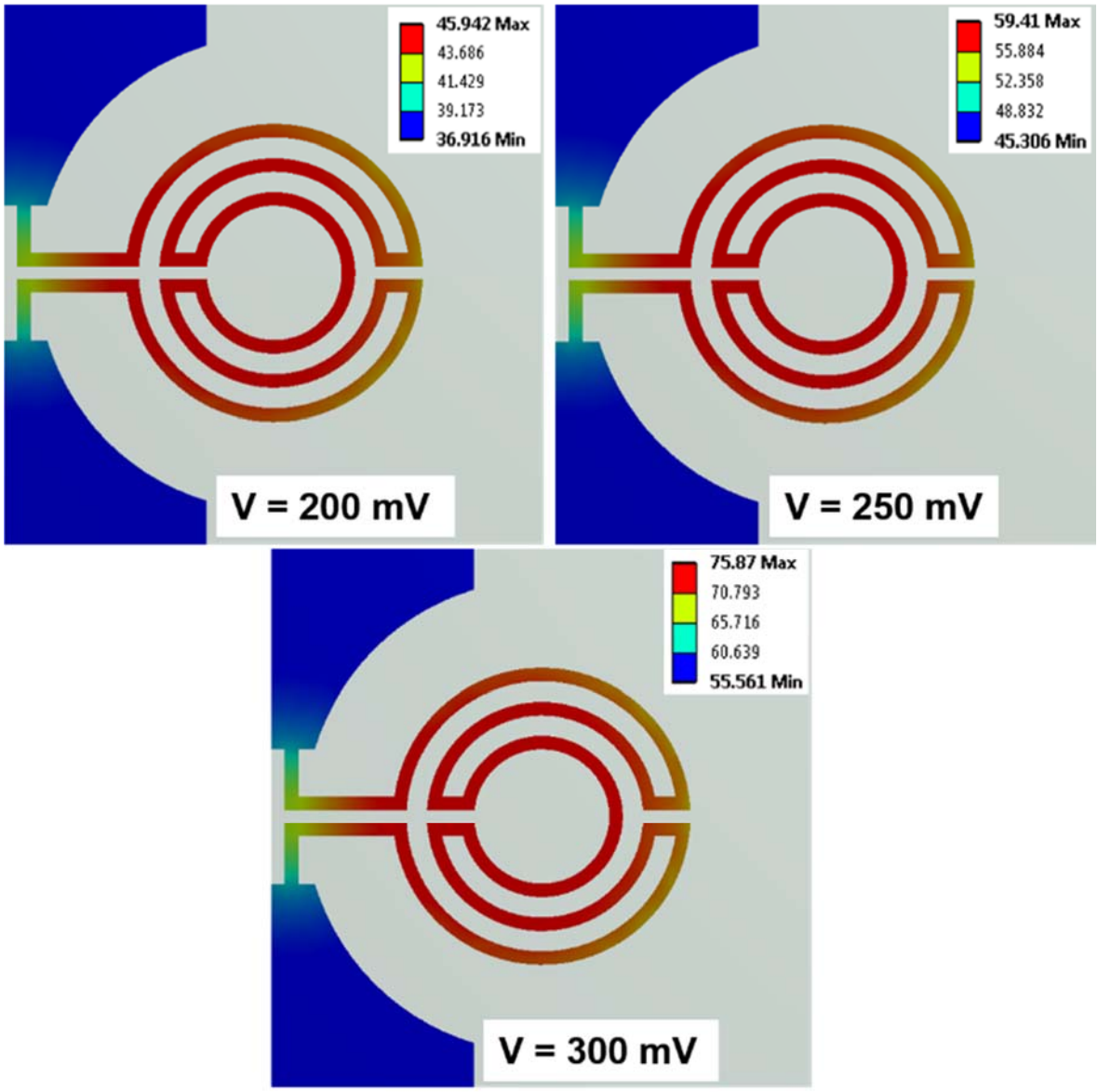

Figure 4.6 Simulation results for temperature of the microheater at time t=1 s for actuation voltages of 200 mV, 250 mV and 300 mV. The heat is localized and uniformly distributed in the heating element within a tolerance of 6.66%.

To be able to accurately track the temperature of the microheater and continuously adjust the temperature to match the set point, both the heater and sensor were calibrated. To calibrate the heater and the sensor, each of their resistances was measured against the reference temperature of a hot plate. The resistances were noted for set points between 20^0C and 75^0C during both - heating and cooling cycles. The solid lines in Fig. 4.7 indicate the fitting curves to account for hysteresis

between heating and cooling cycles. This is the calibration plot used for the feedback control of the temperature of the microheater.

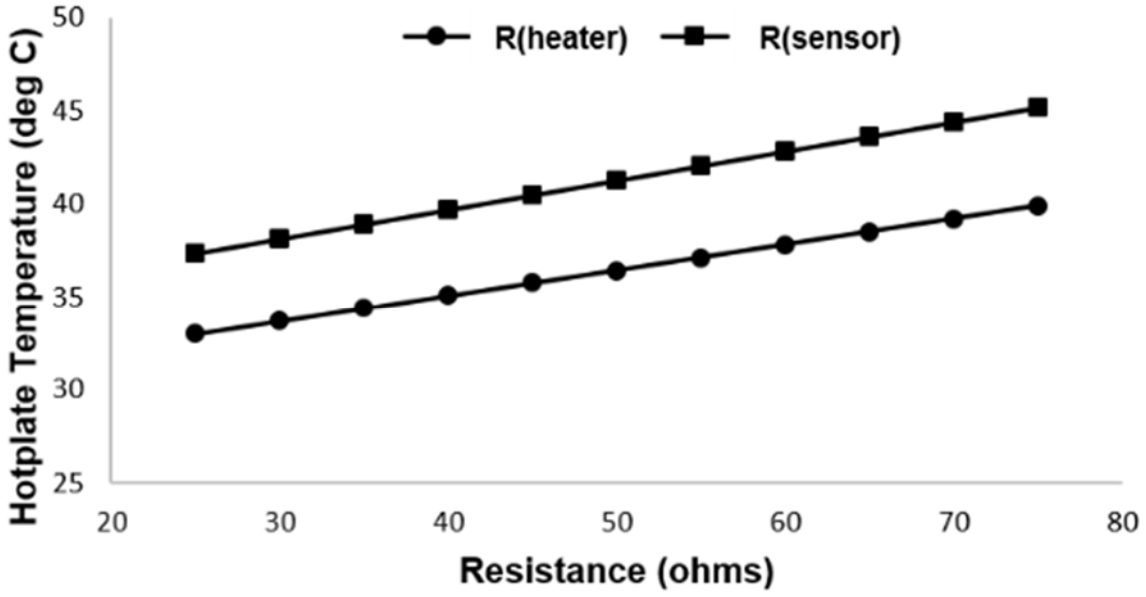

Figure 4.7 Calibration curves for heater and sensor resistances

4.4 Polarizer

The presence of bodily fluids in the body makes the internal organ surfaces highly reflective, resulting in a glare while imaging them [5]. Glossy or highly reflecting surfaces often reflect a linearly polarized component of the incoming light much more strongly than the others. Therefore, our approach to addressing this challenge was to integrate a polarizer in front of our tunable-focus lens. We fabricated a linear polarizer oriented so as to block the reflected linear component. Such selective transmission of incident light based on the plane of polarization enhances the contrast of objects against the background, especially in low light conditions such as a surgical cavity.

A thin film PVA polarizer, shown in Fig. 4.8 was fabricated on a flexible substrate and integrated in front of the camera. A cleaned glass substrate surface was first mechanically etched to pre-define the orientation of the subsequently made polarizing film. A pre-polymer of doped Polyvinyl Alcohol (PVA) was then spin-coated on at 1500 rpm for 1 minute onto the glass substrate (thickness ~ 500 μm). The surface was heated at 100 ^{0}C for 20 minutes to evaporate the solvent and cure the PVA thinfilm. The PVA thinfilm was subsequently peeled off the glass substrate. A PDMS elastomer was then mixed with a curing agent in 10:1 ratio by weight. The mixture was then placed in the vacuum chamber to extract air bubbles. It was then poured onto two glass slides, cured at 80 ^{0}C for 4 hours and then peeled off to yield two flexible PDMS films (thickness ~ 250 μm). The PVA thinfilm was then sandwiched and bonded between the two thin PDMS films to yield the flexible linear polarizer film.

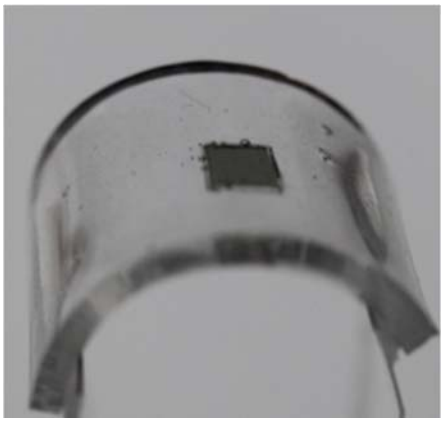

Figure 4.8 Calibration curves for heater and sensor resistances

To test the selective transmission of incident light when passed through the polarizer, we passed a linearly polarized HeNe laser beam (λ=630 nm) through the polarizer. The polarizer was rotated to vary the angle of the incident polarization with respect to the polarizer. It can be seen from Fig. 4.9 that maximum light is transmitted when the incident light is aligned in the same direction as the polarizer and polarization perpendicular to the polarizer orientation is completely blocked.

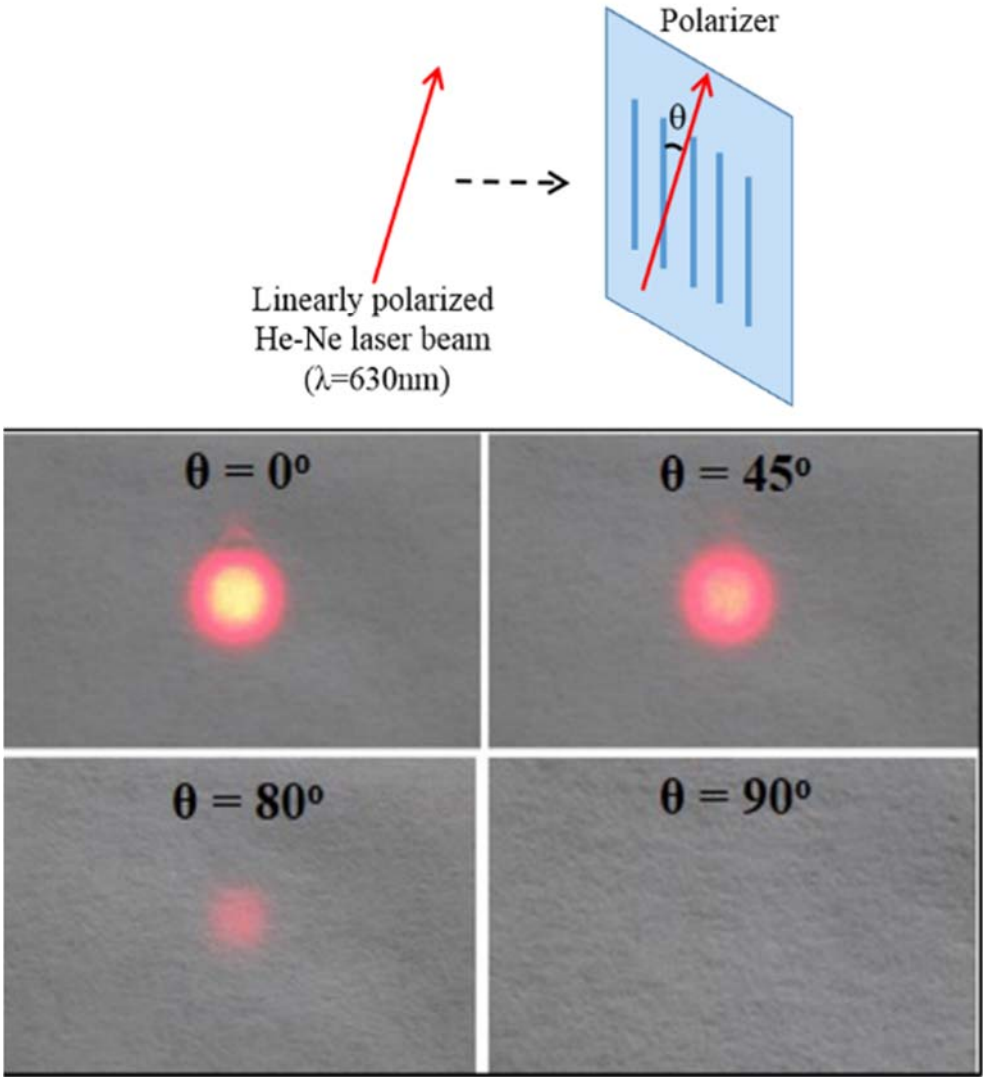

Figure 4.9 Selective transmission of a linearly polarized He-Ne laser (λ=630 nm) when passed through the polarizer.

4.5 Mechanical actuation assembly

The trocar-camera assembly (TCA) consists of four microcameras assembled symmetrically around a surgical port/trocar, connected together by a mechanical structure. The mechanical design of the assembly is similar to the frame of an umbrella. It has four metal arms, each supporting an assembled microcamera unit, connected together by a hub around the periphery of the distal end of the pole. These arms are connected by ribs or 'stretchers' to another hub (the 'runner'). The runner can freely slide along the trocar, which in turn controls the upward/downward motion of the arms. For instance, as the runner slides up the trocar, the stretchers extend thus raising the arms to which they are attached. The position of the runner along the trocar is controlled by a slider crank mechanism. The radius of the crank and the length of the connecting rod define the range of angles of orientation of the camera arms. The rotational speed of the crank is controlled by a dc motor coupled with a two stage gear reduction. Gears are used with the dc motor to lower the motor's speed while increasing the output torque.

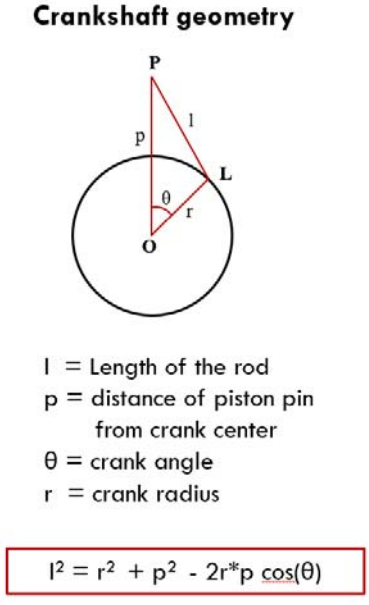

Figure 4.10. Crankshaft actuator design calculations

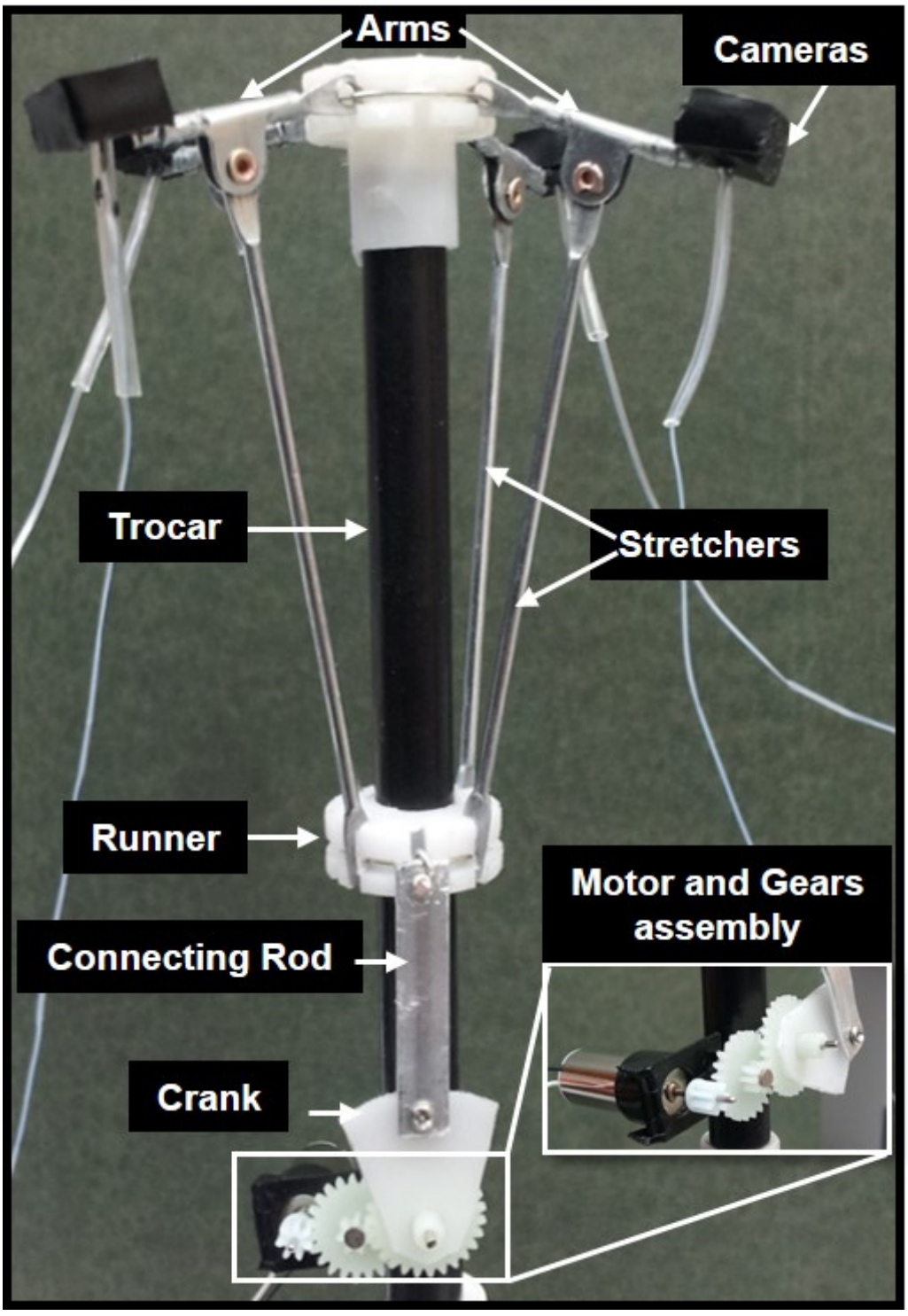

Figure 4.11 Different parts of the trocar-camera assembly. (Inset) shows a close-up of the dc motor with a two-stage gear reduction set.

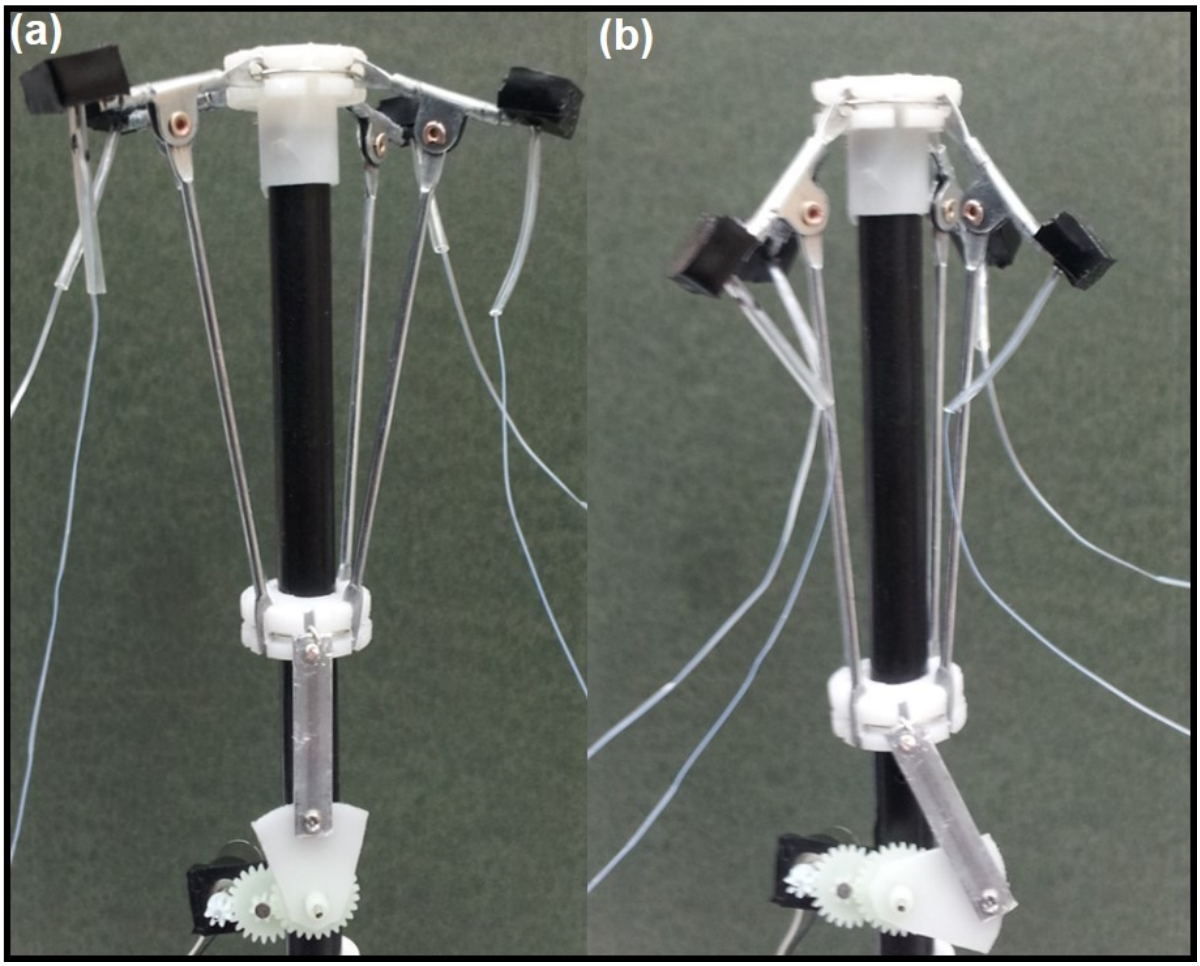

Figure 4.12 (a-b) Actuation of the TCA. As the crank rotates clockwise, the connecting rod pulls the runner downwards. As the runner slides down the trocar, the stretchers pull the arms closer to the trocar.

4.6 Graphical User interface

A graphical user interface was designed using the LabVIEW (National Instruments Inc., Austin, TX, USA.) programming environment, to provide unified controls for focus tuning, image acquisition and illumination controls. The heater, sensor and the light source were monitored and controlled using the CompactDAQ chassis cDAQ-9172 in conjunction with the analog input module, NI 9201 and the output module, NI 9264. A closed-loop temperature control was

implemented for the integrated heater-sensor device. The image acquisition and visualization from the cameras was done directly via the sensor USB board.

4.7 Imaging results

The effects of integration of a polarizer in front of the camera while imaging reflective surfaces were tested by placing a highly reflective metal nail in the center of the scene being imaged. Fig. 4.13 demonstrates effective glare reduction while imaging with the use of a polarizer.

Figure 4.13 Reduction in glare with the use of a polarizer as seen from comparison of an image without using a polarizer in front of a tunable camera (left) and the same image captured with a polarizer in front of the lens (right).

To test the optical focusing capabilities of our cameras, the position of a single tunable camera was fixed 12 cm away from the test scene. The test scene comprised of a periodic arrangement of 9 dice (1.5 cm × 1.5 cm × 1.5 cm) forming a rhombus (length = 16 cm). Images of the scene were then captured by the camera while varying the temperature from 45 0C to 65 0C to tune the lens. Fig. 4.14 shows a series of three images captured by a camera while tuning the

thermo-responsive lens using a microheater. The scene is first out of focus; then the camera gradually focuses in on the scene as the lens is tuned.

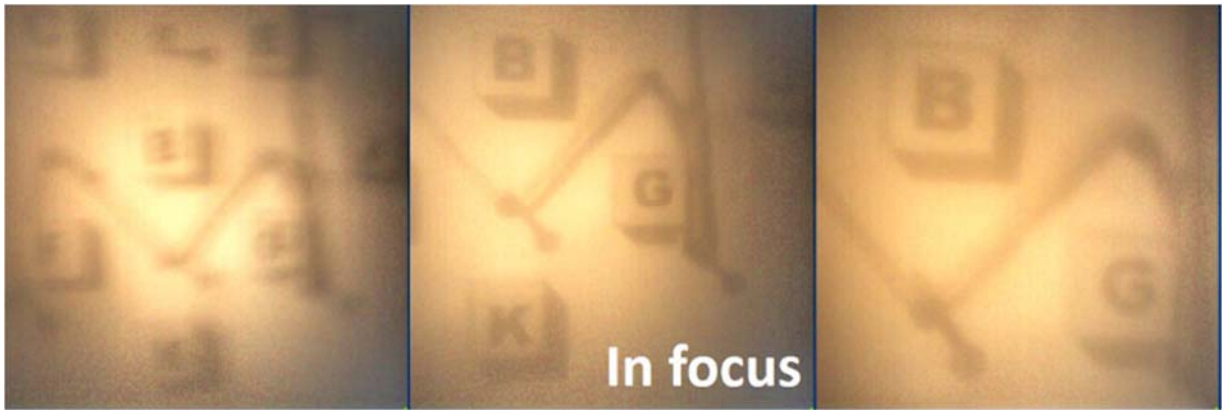

Figure 4.14 Images of a test scene as captured by a single camera while the focal length of its tunable liquid lens was being tuned using a microheater.

Commercial laparoscopic trainer boxes are often used to develop laparoscopic skills, using inanimate tasks, in novice surgeons. A common training task assignment is to stretch a rubber band around nails tacked on a board [5]. We modeled our test surgical scene to closely mimic this training setup, as shown in Fig. 4.15 (e). The test scene was placed in a dark environment with illumination provided solely with a fiber optic light guide to closely resemble a surgical cavity. Since the NanEye image sensors do not have an IR filter, an IR cut was placed at 680nm to filter the incident light for faithful color imaging.

To test the implementation of our imaging setup in the mock surgical scene, the test scene was sealed within a box with a small opening, similar to an incision in a surgical cavity. The TCA assembly was introduced into the scene along with a fiber optic light guide for illumination. During insertion, the mechanical arms (with the microcameras) were in a closed configuration with the arms parallel to the sidewalls of the port. Once the surgical port was positioned, the arms of the frame were flared out. Initially, the orientation angle of the array was adjusted to provide the

desired viewing perspective, depth of field and horizontal field of view. Finer adjustments were then made to ensure distinct but slightly overlapping sub-scenes, as seen by individual cameras. In our design, the orientation angle of all the microcameras can be simultaneously adjusted within an error margin of 5°.

First, the camera lenses were tuned individually to obtain focused images of each of their sub-scenes. This independent optical tuning feature enables our imaging system to handle different object distances without affecting the overall depth perception of the scene. So sharp images of all the sub scenes are obtained by individual cameras as seen in Fig. 4.15 (a-d). These scenes were then stitched together in a commercial software PTGui^{TM} to obtain a panoramic image shown in Fig. 4.15 (e). As seen from the figure, this yields to enhanced depth perception and a significantly large field of view of 128^{0}, which is greater than that of any of the individual source images.

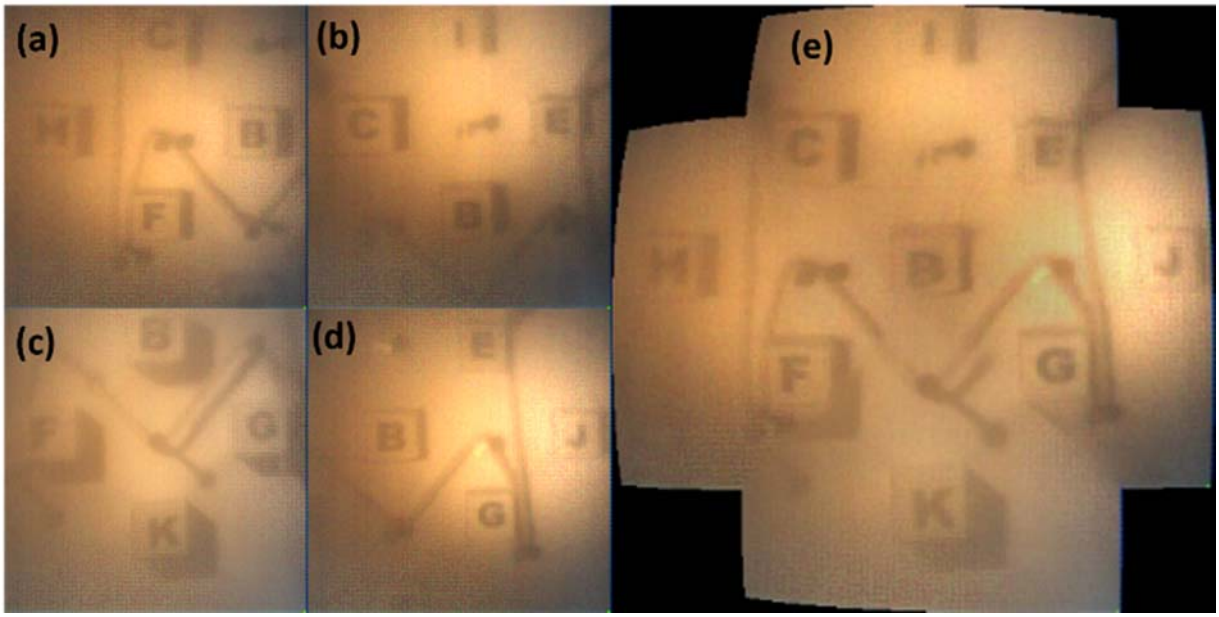

Figure 4.15 Images of a mimicked surgical scene as captured by our camera array. (a-d) Sharp images of all the sub scenes were obtained by individual cameras These scenes were then stitched together in a commercial software, PTGui^{TM} to obtain a very large field of view compared to any single camera alone (e).

All the images in Fig. 4.13-4.15 are unprocessed, raw images. that suffer from low brightness levels, as shown in the histogram in Fig. 4.16 (a). However even some preliminary post processing of the intensity levels of the histogram can significantly improve image quality, as seen in Fig. 4.16(b-c). The vignetting seen around the edges in individual camera images can be attributed to variation in illumination intensity with change in camera orientation. Also, image distortion can be observed in the panorama in Fig. 4.15(e) that is not seen in any of the sub-scene source images. However, this is primarily due to limitations of the commercial software.

To demonstrate the enhancement in depth perception with the multi-camera array, we imaged a scene with two tubes placed one behind the other, separated by a distance of 10 mm. The scene was imaged with all four cameras of the TCA at an arbitrary orientation angle. As can be seen in Fig. 4.17, while imaging the scene with a single camera, the depth-wise separation of different objects may (Fig. 4.17(c) - (d)) or may not (Fig 4.17(a) - (b)) be apparent. However, while imaging with our multi-camera array, the same scene can be viewed from four different viewing perspectives thus leading to increased information about the relative positions of the two objects.

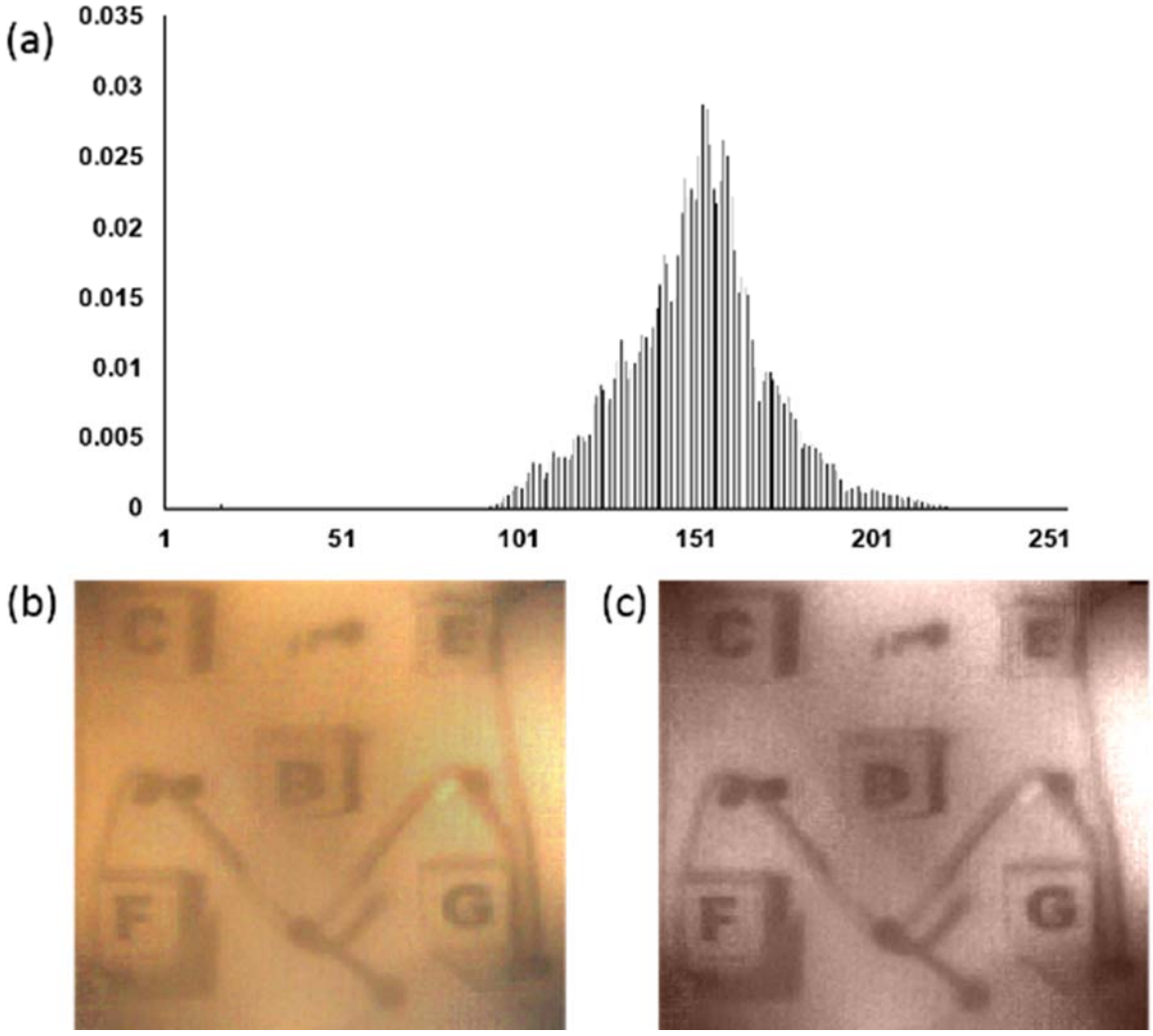

Figure 4.16 (a) Pixel intensity distribution (histogram) of the panoramic image in Fig. 16 (e). (b) Cropped panoramic image before processing (c) Cropped panoramic image after redistribution of the intensity levels in the histogram.

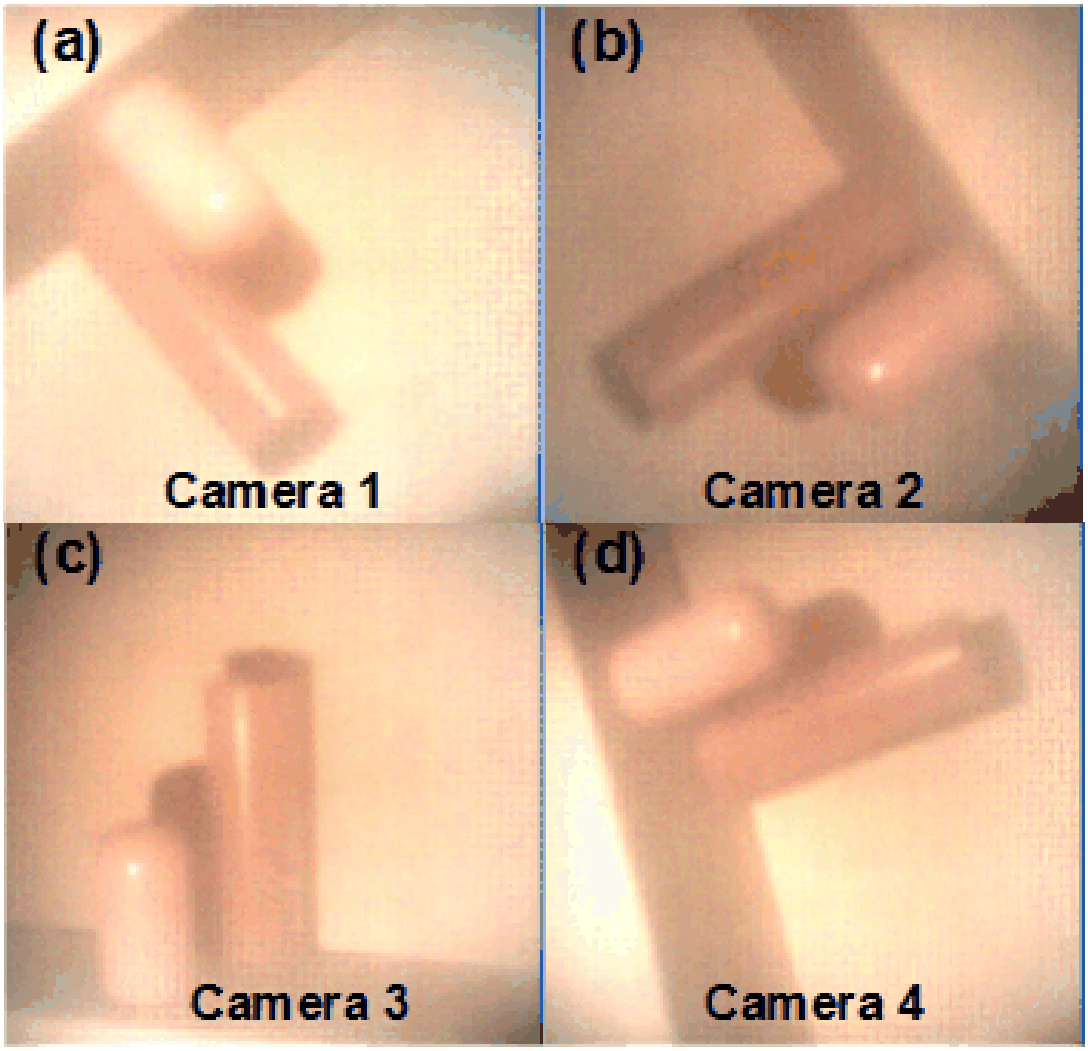

Figure 4.17 Enhanced depth perception due to multi-camera array. Images of two tubes (Ø=15 mm) separated by a distance of 10 mm, as captured by four cameras in the TCA. Imaging the same object with a multi-camera array yields depth cues from four different viewing perspectives, leading to an enhanced depth perception compared to any single camera alone.

References

[1] http://www.surginno.com/laparoscopic-surgery

[2] http://www.melakafertility.com/laparoscopy.shtml

[3] C.F. Chau and T. Melvin, “Design and fabrication of a quasi-ordered nanoporous silicon membrane suitable for thermally induced drug release,” *J. Micromech. Microeng*. , vol. 22, no.8, 2012.

[4] E.W. Abel, Y. Zhuo, P.D. Ross, and P.S. White, “Automatic glare removal in endoscopic imaging,” *Surg Endosc*., vol. 28, no. 2, pp. 584-591, 2014.

[5] R. Lu, S. Liu, X. Luo, and B. Zhang, "Thermal safety analysis of Capsule Endoscope,” *7th ICEPT '06*, Aug. 26-29, 2006, pp. 1-4.

[6] E. Hiemstra, W. Kolkman, M. A. van de Put, and F. W. Jansen, “Retention of basic laparoscopic skills after a structured training program,” *Gynecol Surg*., vol. 6, pp. 229–235, 2009.

5 Remote axial focusing using tunable lenses in 3D microscopy

5.1 Introduction

Microscopy is one of the most widely used tools by biologists to study various cells, organisms as well as for some *in vivo* applications. Conventional microscopes illuminate the entire sample area and collects light from the sample in a single snapshot. This technique collects signal coming from all depths in the sample, and so out-of-focus light can cause substantial blurring. For a volumetric visualization of the sample or to enable depth scanning along the axial direction, it is necessary to move the sample relative to the fixed focal plane of the microscope objective. For this purpose, a mechanical z-scanning stage is typically employed. The stage enables the focal plane to move through the sample. To obtain volumetric images, various axial scanning mechanisms have been implemented [1]. Typical approaches used to achieve axial scanning are a motorized stepper stage or a piezoelectric stage. While stepper motors offer the advantage of unlimited travel distance, they suffer from hysteresis. Piezoelectric stages on the other hand, help eliminate hysteresis at the cost of the travel distance which is reduced to 100-200 μm. Both the types of stages, however, are bulky and cause vibrations and wobble in the sample due to high inertia [14]. Additional care is required to avoid mechanical overshoots and backlash from the tip touching the sample. Additionally, for water or oil-immersion lenses, vibration of the sample stage can cause disturbance or ripples in the immersion media that can lead to significant distortion in the images. Some of the techniques employ translation of the sample or the objective lens relative to the other [2,3], whereas others utilize movement and shaping of focus and/or wavefront by exploiting chromatic aberrations [4,5], using adaptive phase compensation techniques [6-8], or utilizing a variable focal length lens [9-13].

A robust alternative to the use of mechanical scanning stages is a remote focusing system that allows both the objective and the sample to be stationary. One such solution is the employment of a tunable-focus liquid lens in conjunction with a microscope objective to achieve axial scanning through a sample being imaged. Our work demonstrates the implementation of a robust, cost-effective and energy-efficient axial tuning solution for 3D microscopy based on thermos-responsive hydrogel-based tunable liquid lenses.

5.2 Principle of operation

The focus-tunable liquid lenses used in our system are thermo-responsive hydrogel based liquid lenses. The lens is defined by an interface between two immiscible optical liquids with different refractive indices but closely matching densities, typically water and oil. The lens meniscus is manipulated by changing the volume of water on one side of a pinned liquid-liquid interface. This change in volume is achieved by expansion or shrinkage of a smart hydrogel ring structure surrounding the water chamber, in response to an ambient temperature change. The lens structure is modelled based on our previous publications.

When the tunable liquid lens is placed in the optical path between the incoming light beam and a microscope objective, the lens alters the incident beam divergence as its focal length changes. The result is a shift in the focal plane along the axial direction, ±z-axis depending on the focal length of the lens. By controlling the focal length of the lens, we can image at different depths within the sample.

5.3 Experimental

5.3.1 Optical configurations

Microscope objectives are mostly designed to be telecentric in object space. Telecentric are space invariant and linear. Space invariance implies constant lateral and longitudinal magnification throughout the sample space and that the shape of the point spread function (PSF) is independent of the absolute location of the point source [16]. In other words, the out-of-focus planes are not 'zoomed in' or 'magnified' while imaging a thick sample. Fig. 5.1 illustrates the difference between axial scanning in a non-telecentric system vs that in a telecentric optical setup.

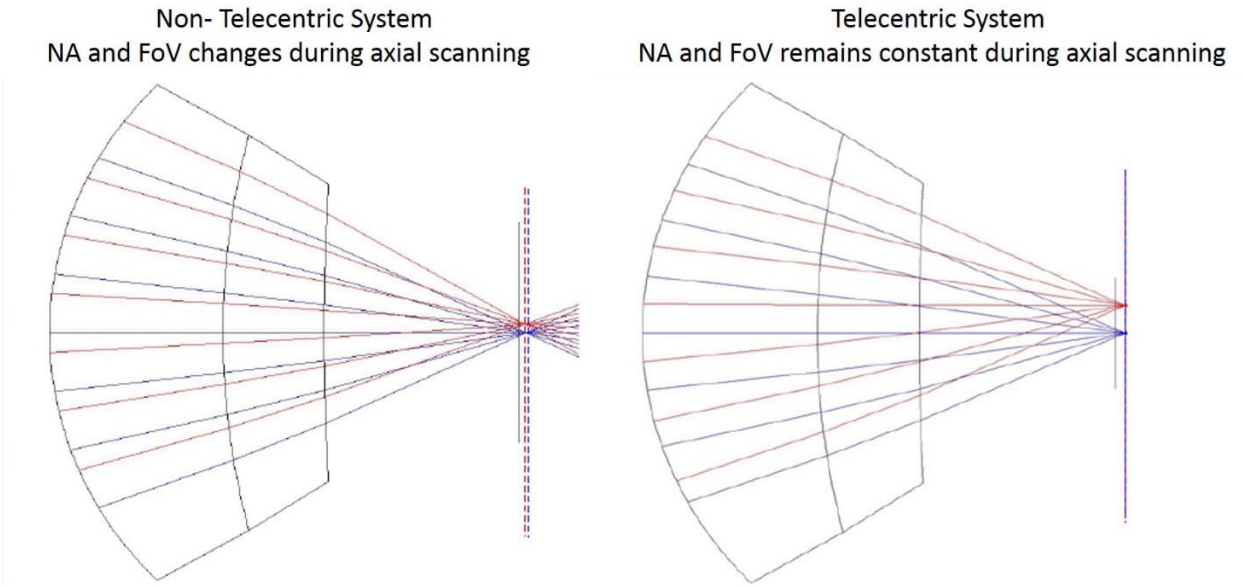

Figure 5.1 Non-telecentric systems cause change in magnification and hence field of view during axial scanning whereas the field of view is maintained constant in a telecentric optical setup [11].

While designing a tunable microscope objective using a tunable liquid lens and a commercial objective, the best way to preserve telecentricity is to use a 4f relay lens pair to relay the image of the pupil plane of the objective and align the tunable lens at this conjugate pupil. However in the case of our system, it is not possible to align the tunable lens accurately at the

conjugate pupil position. Hence the tunable lens was aligned as close to the rear stop of the objective lens as possible.

5.3.2 Optical Setup

A 632.8 nm randomly polarized laser (HNL050R, Thorlabs Inc., Newton, NJ) is used for illumination. The output power of the laser is 5mW and has a 0.81 mm beam diameter ($1/e^2$). The beam expander stage comprises of a commercial 3x beam expander (BE03M-A, Thorlabs Inc., Newton, NJ) and a 3.33x afocal lens pair (AC254-030-A and AC254-100-A, Thorlabs Inc., Newton, NJ). The beam expansion stage is designed to ensure that the size of the beam incident on the microscope objective was greater than the pupil diameter (8mm). This is essential to ensure uniform illumination of the objective and hence optimal imaging. To reduce the spatial coherence of the laser beam, a rotating optical diffuser is placed in the Fourier plane of the afocal lens pair after the beam expander. The grit rating of the optical diffuser used was determined on the basis of size of the finest features in the sample being imaged. The expanded beam is then passed through an adjustable iris diaphragm before deflected onto the tunable lens using a beam splitter. The variable iris/aperture controls the width of the bundle of light rays to eliminate excess light that can cause glare and reduce contrast. A 5 mm aperture tunable lens was used to alter the beam divergence at the back focal plane of a water-immersion microscope objective (CFI Apo 40XW NIR, Nikon). The tunable lens was mounted in a custom-made PDMS alignment ring placed and encapsulated by a polyimide insulated flexible heater with a power density of 10 W/in^2 at 28V (Kapton KHLV-0502/10, Omega Engineering Inc., Stamford, CT, USA) to vary the lens temperature. To facilitate precise centering of the tunable lens with the optical axis of the objective, the tunable lens was mounted in an x-y translation mount. Centering of the tunable lens with the optical axis is critical to avoid lateral shifts in the image of the sample. The detection arm

consists of a lens (AC254-200-A, Thorlabs Inc., Newton, NJ, USA) focusing light onto an image sensor (AVT Stingray IEEE1394 C-Mount Cameras, Allied Vision). Fig. 5.2. outlines the ray tracing diagram of the optical setup of our microscope and Fig. 5.3. illustrates a 3D representation of the actual setup.

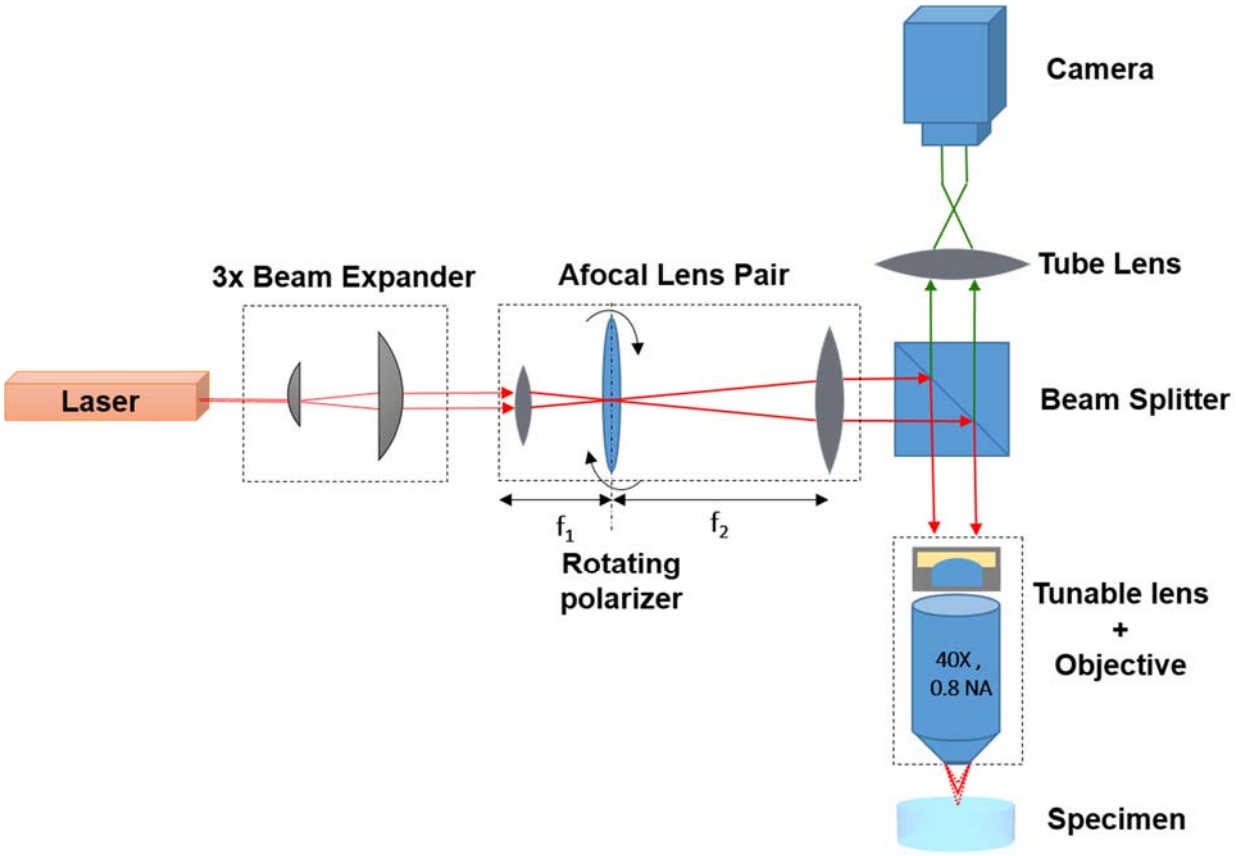

Figure 5.2 An optical ray tracing diagram of the setup of our 3D microsope. A 0.81mm diameter He-Ne laser beam is first expanded by a 9x beam expander before being deflected onto a tunable lens-objective combination that focuses the light at different depths of a sample depending upon the focal length of the tunable lens. The detection arm consists of a tube lens which focuses light to produce an image on an image sensor.

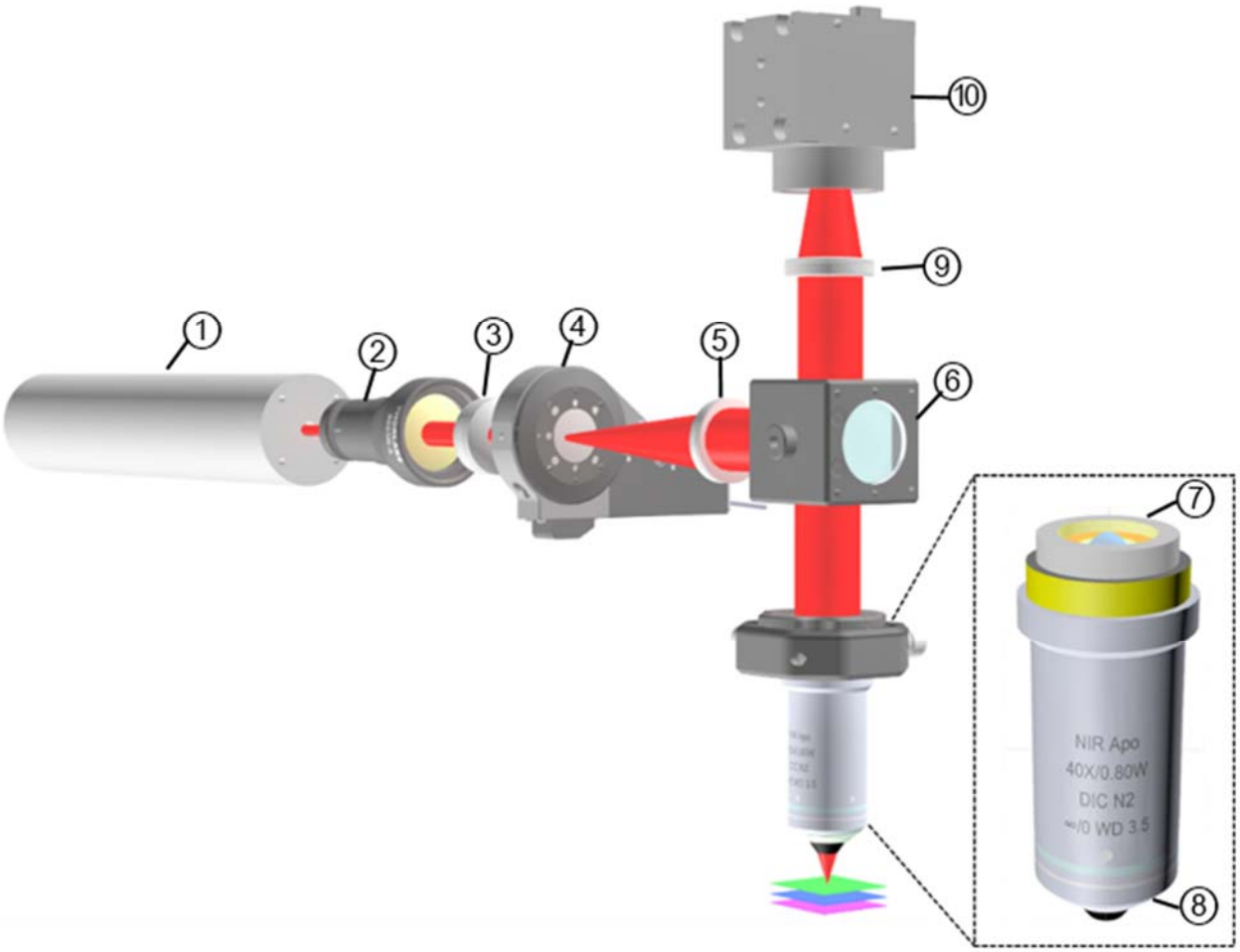

Figure 5.3 A 3D representation of the actual optical setup of the 3D microscope with remote axial focusing achieved by a tunable liquid lens placed close to the rear stop of a microscope objective.

5.3.3 Optical modelling

We used the Zemax (Bellevue, WA, USA) software package to simulate the light propagation through the tunable lens-objective combination and to test the performance of our 3D microscope. The multi-configuration editor was used to define the different radii of curvature of the liquid lens corresponding to different temperatures. An edge thickness constraint was placed on surfaces of either side of the lens surface to simulate the pinning of the liquid-liquid lens interface. The

dimensions of lens chambers were optimized using a merit function to minimize the RMS spot size at the image plane.

The microscope objective used in this setup is Nikon CFI APO NIR Objective; water immersion objective with 40x magnification, numerical aperture 0.8 and working distance of 3.5mm. Sufficient prescription data of the microscope objective is not available for ZEMAX simulations. Aspheric lenses are widely used to model and predict the optical performance of a commercial microscope objective. In our ZEMAX simulations, a model of another commercial objective closely matching the characteristics of the one used in our system (40X, 0.8NA, 2.5mm WD) was designed based on the prescription data found in a patent [17]. Nikon CFO APO objectives are designed for a 200mm tube lens. Given that the magnification of the objective is 40X, the focal length of the objective is given by $f_{objective} = f_{tube}/M = 5mm$.

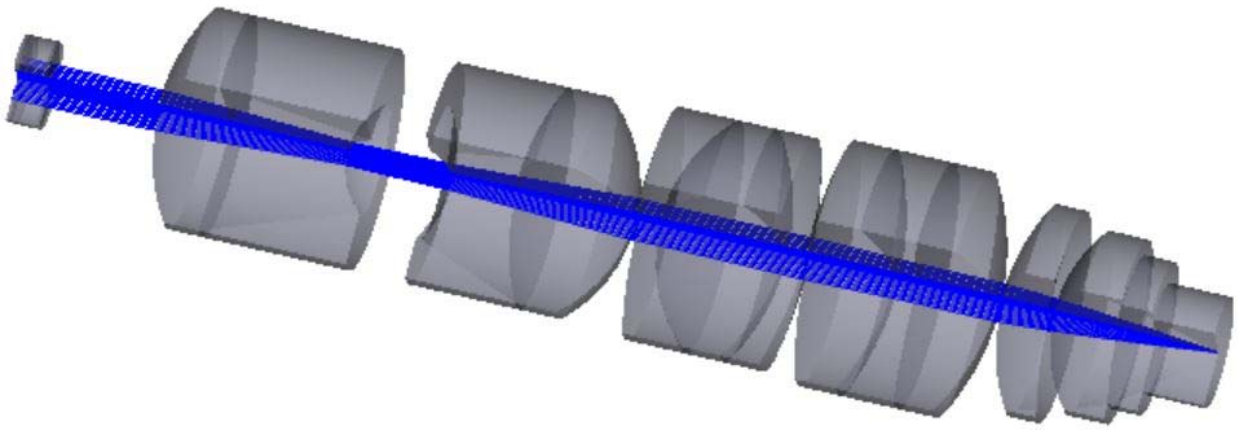

Figure 5.4 A shaded model drawing of a 3D layout of a tunable liquid lens and a commercial microscope objective, as designed in ZEMAX optical modelling software.

5.4 Results and discussion

5.4.1 Lens Calibration

We used a batch fabrication process to increase efficiency and accuracy of the lens molds. 3D molds were designed using the modelling software 3DMax and were printed using Stereolithography as shown in Fig. 5.5. The actual lens design was similar to that outlined in Chapter 3.

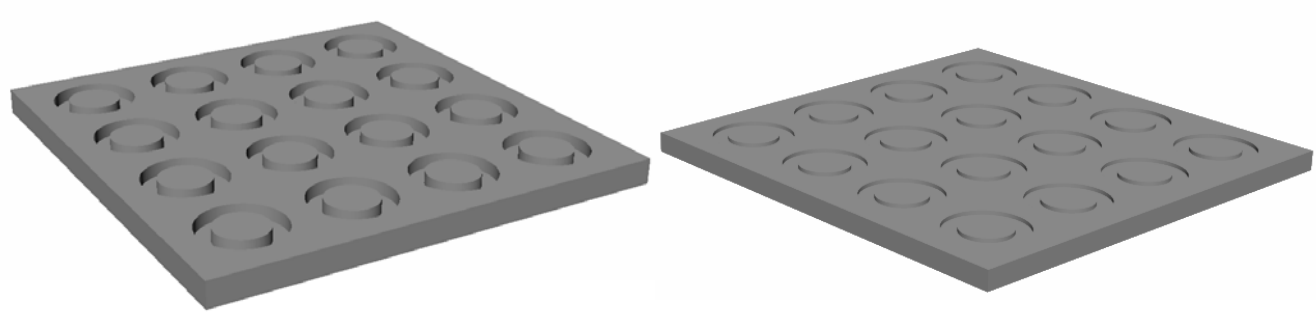

Figure 5.5 3D schematics of batch fabrication molds used in the fabrication of lens containers. These molds were 3D printed using stereolithography.;

The lens design is flexible and allows for changing the range of focal length tuning range by changing the original volume of water filled in the water container at 32˚C. For our experiments, we designed our lenses to tune from focal lengths of -30mm to -∞ and from 45mm to +∞. Depending on the initial water volume, the tuning range can be adjusted to obtain images from a symmetric focal shift on either side of the native focal plane or only on one side of the native focal plane. This gives our system an added degree of flexibility and adaptability for imaging systems designed for different biological systems. Fig. 5.6. shows the temperature vs focal length plot for a sample lens.

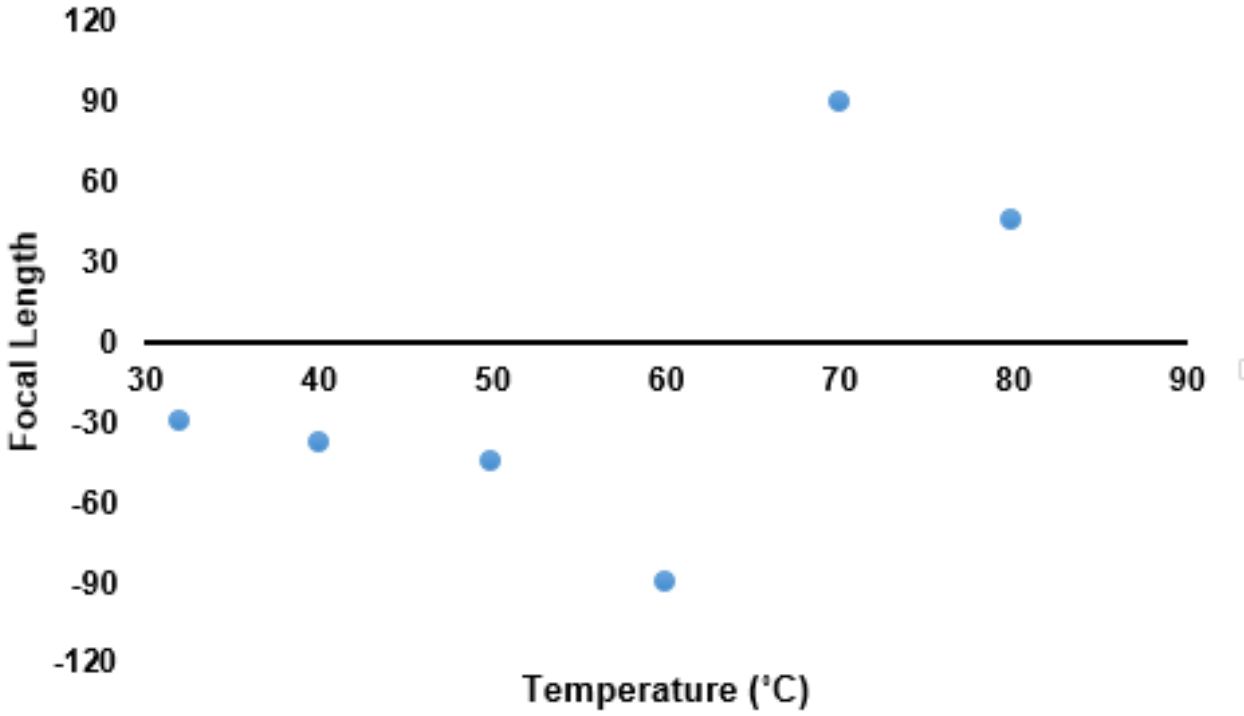

Figure 5.6 Plot showing the variation of the focal length with respect to the ambient temperature of a tunable liquid lens. As the temperature is varied from 30 degrees to 90 degrees , the lens tunes from concave focal lengths of -30mm to -∞, then switches to a convex lens from focal lengths of +∞ to 45mm.

5.4.2 Characterization

5.4.3 Axial tuning

To test the focusing range of our setup in the axial direction, a USAF 1951 target was used as an imaging sample. The axial position of the target was varied by ±750 µm with respect to the original focal plane of the microscope objective(working distance = 3.5mm), in steps of 50 µm using a precision translation stage (MT3, Thorlabs Inc., Newton, NJ). At each step, the focal length of the liquid lens was changed to test for capability to focus the target at the new axial distance. The axial focusing range was empirically calculated to be 1.5 µm. The axial scanning range of the tunable lens-objective combination was also simulated in ZEMAX.

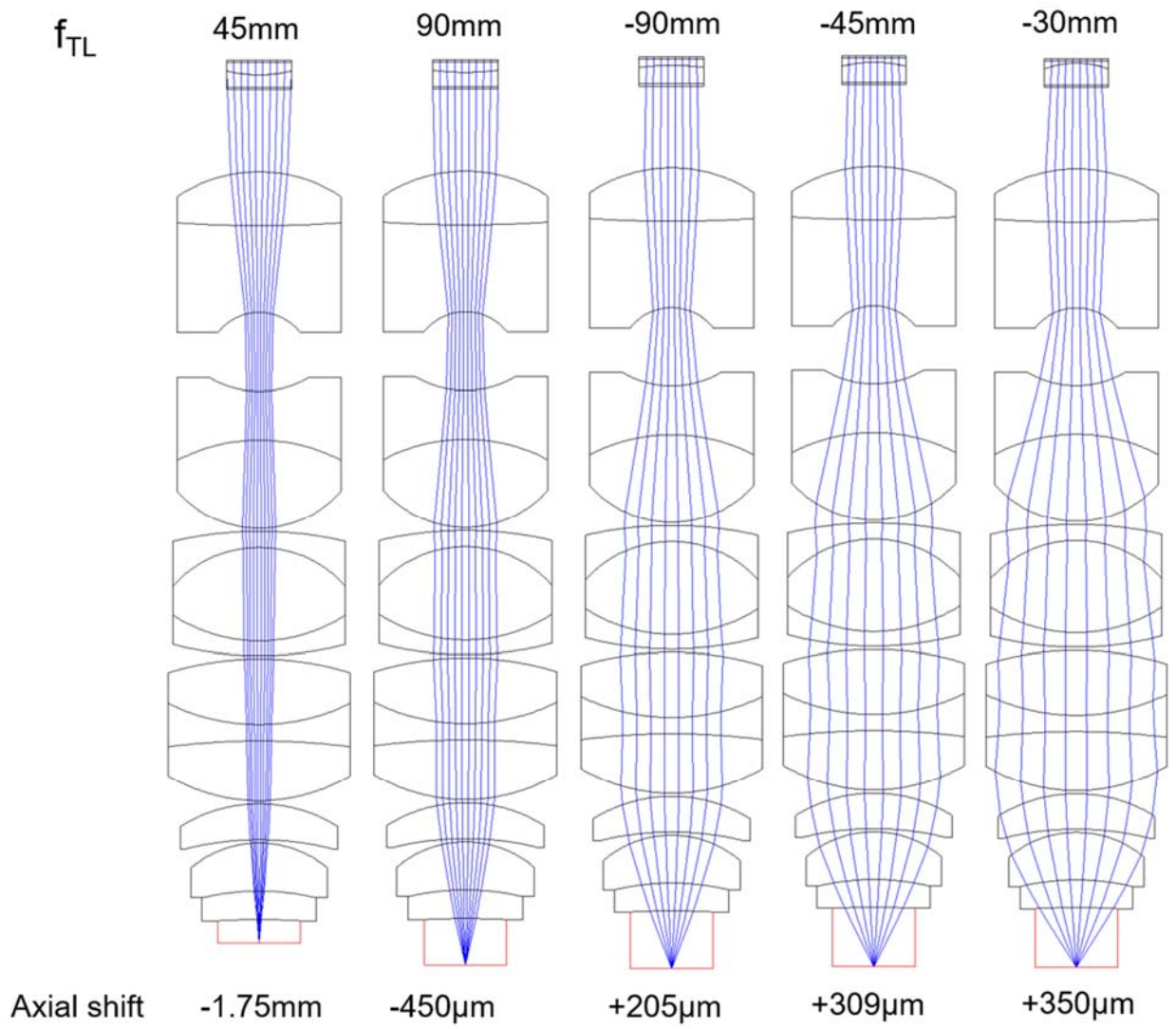

Figure 5.7 ZEMAX simulations showing the axial shift of the native focal plane with a change in the focal length of the tunable lens

5.4.4 Field of View and Numerical Aperture

In our setup, the tunable lens is placed at a finite distance from the rearstop of the microscope objective which lies inside the mounting shoulder and is inaccessible. As a result, the system has an angular (non-constant) field of view. In other words, the system is non-telecentric and exhibits different fields of view at different axial positions. Another interpretation of this is that the numerical aperture of the system changes as the axial position of the focal plane is changed. To

quantify the change in the field of view, we imaged a US Air Force 1951 target placed on a z-axis translation stage at different axial positions. The sample was moved through the axial tuning range (±750µm) with respect to the original focal plane of the objective. The field of view was found to vary between 240µm to 420µm in contrast with the native field of view of 625µm.

5.4.5 Aberrations and resolution

To estimate the aberrations of our optical system, the Modulation Transfer Function (MTF) of the tunable lens-objective combination was calculated for different focal lengths of the tunable lens. The MTF is a measure of the ability of an optical system to transfer contrast from the subject to the image plane, as a function of spatial frequency. Fig. 5.8 shows a comparative plot of MTFs as the liquid lens is tuned from -30 mm to +90 mm focal length.

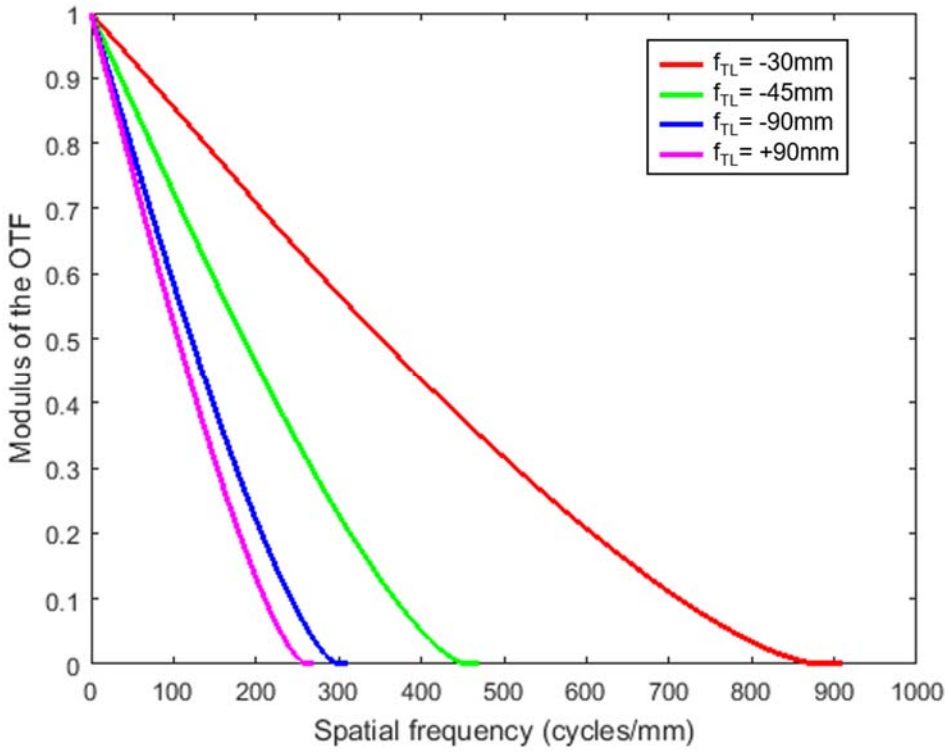

Figure 5.8 A plot of the Modulation Transfer Function as derived from ZEMAX for various tunable lens focal lengths. A reasonable contrast of more than 20% is observed for spatial frequencies above 200 cycles/mm.

To demonstrate the axial tuning capabilities of our system, we imaged microspheres in double-layer stacked microfluidic channels. A 0.15 mm thick coverslip is placed on top of the device. Both the microfluidic channels are 250 µm wide and 250µm deep and are separated by a 100 µm layer of PDMS. 20 µm polystyrene beads were flown into the lower microchannel whereas the top microchannel has 40 µm beads. To image the entire microfluidic sample, we needed to achieve an axial focusing shift of 750 µm from the top of the specimen. Fig. 5.5 shows images taken during an axial scan of this microfluidic device.

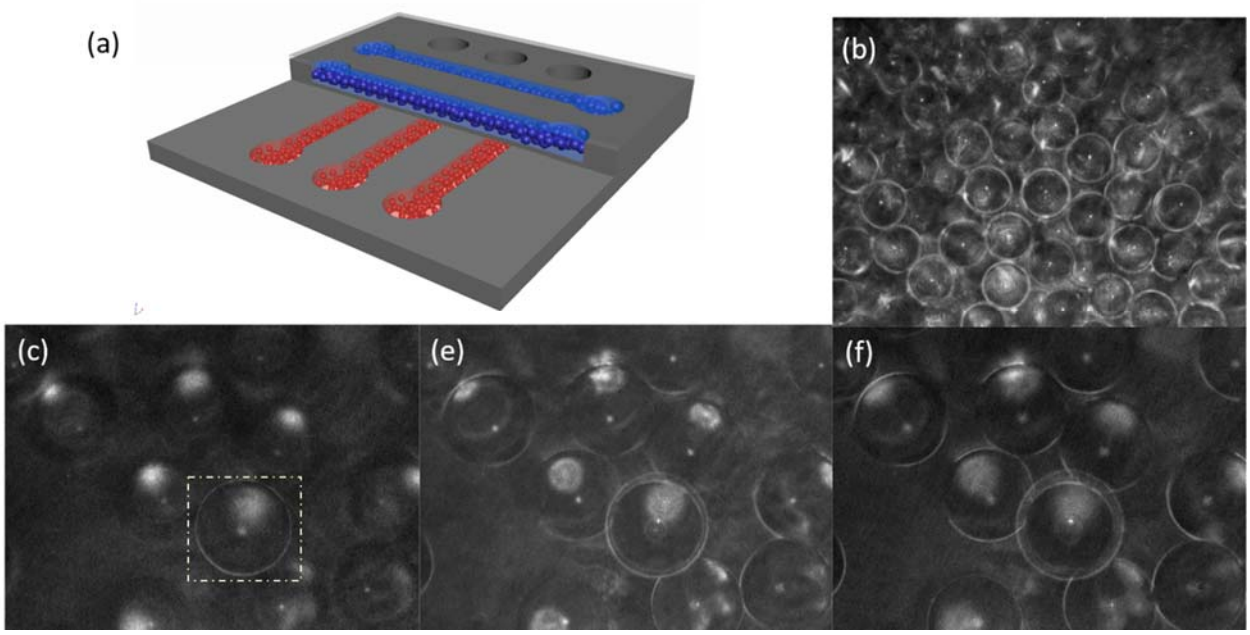

Figure 5.9 Demonstration of axial focusing of the 3D microscope using a microfluidic channel. (a) Schematic of the microfluidic device used for imaging. It consists of 2 layers of microfluidic channels with microspheres flown through them. (b) shows images of the 20 µm beads in the lower channel (c)-(d) shows focusing on multiple layers within the top microfluidic channel containing 40 µm beads

5.4.6 Evaluation of system – Live Cell imaging

To demonstrate the operation of our microscope, we imaged Spodoptera frugiperda (Sf21) cells suspended in a microfluidic channel. The sample contained cells with an average size of 15-18μm and a cell density of $1x10^6$ cell/ml. The cells were pipetted into a microfluidic chamber and a __mm thick coverslip was placed on top of the sample to enable imaging with a water-immersion objective. The temperature of the lens was varied from 30 to 70C. Three images of the sample were captured at three different focal plane. The images obtained from the camera were then post-processed in MATLAB to enhance contrast.

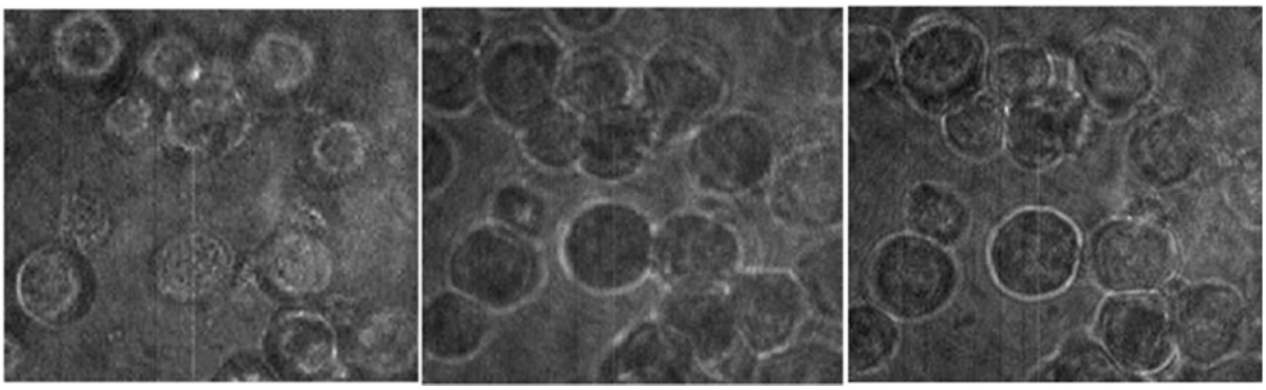

Figure 5.10 Images of SF21 cells as captured by our 3D microscope along different axial positions of the focal plane.

References

[1] J. M. Jabbour, M. A. Saldua, J. N. Bixler, and K. C. Maitland, "Confocal endomicroscopy: instrumentation and medical applications," *Ann. Biomed. Eng*. 40(2), 378–397, 2012.

[2] A. A. Tanbakuchi, A. R. Rouse, J. A. Udovich, K. D. Hatch, and A. F. Gmitro, "Clinical confocal microlaparoscope for real-time in vivo optical biopsies," *J. Biomed. Opt*. 14(4), 044030, 2009.

[3] K. B. Sung, C. Liang, M. Descour, T. Collier, M. Follen, and R. Richards-Kortum, "Fiber-optic confocal reflectance microscope with miniature objective for in vivo imaging of human tissues," *IEEE Trans. Biomed. Eng*. 49(10), 1168–1172, 2002.

[4] C. Olsovsky, R. Shelton, O. Carrasco-Zevallos, B. E. Applegate, and K. C. Maitland, "Chromatic confocal microscopy for multi-depth imaging of epithelial tissue," Biomed. *Opt. Express* 4(5), 732–740, 2013.

[5] P. M. Lane, R. P. Elliott, and C. E. MacAulay, "Confocal microendoscopy with chromatic sectioning," *Proc. SPIE*, 4959, 23–26, 2003.

[6] A. J. Thompson, C. Paterson, M. A. Neil, C. Dunsby, and P. M. French, "Adaptive phase compensation for ultracompact laser scanning endomicroscopy," *Opt. Lett. 36(9),* 1707–1709, 2011.

[7] E. J. Botcherby, R. Juskaitis, M. J. Booth, and T. Wilson, "Aberration-free optical refocusing in high numerical aperture microscopy," *Opt. Lett.* 32(14), 2007.

[8] S. Kumar, D. Wilding, M. B. Sikkel, A. R. Lyon, K. T. MacLeod, and C. Dunsby, "High-speed 2D and 3D fluorescence microscopy of cardiac myocytes," *Opt. Express* 19(15), 13839–13847, 2011.

[9] L. Yang, A. Mac Raighne, E. M. McCabe, L. A. Dunbar, and T. Scharf, “Confocal microscopy using variablefocal- length microlenses and an optical fiber bundle,” Appl. Opt. 44(28), 5928–5936, 2005.

[10] B. F. Grewe, F. F. Voigt, M. van ’t Hoff, and F. Helmchen, “Fast two-layer two-photon imaging of neuronal cell populations using an electrically tunable lens,” Biomed. Opt. Express 2(7), 2035–2046, 2011.

[11] Optotune Application Note, “Optical focusing in microscopy with Optotune’s focus tunable lens EL-10-30”, Optotune, 2013.

[12] K.-S. Lee, P. Vanderwall, and J. P. Rolland, “Two-photon microscopy with dynamic focusing objective using a liquid lens,” Proc. SPIE 7569, 756923, 2010.

[13] Jabbour, Joey M. et al. “Optical Axial Scanning in Confocal Microscopy Using an Electrically Tunable Lens.” Biomedical Optics Express, 5, 645–652, 2014.

[14] Y. Nakai, M. Ozeki, T. Hiraiwa, R. Tanimoto, A. Funahashi, N. Hiroi, A. Taniguchi, S. Nonaka, V. Boilot, R. Shrestha, J. Clark, N. Tamura, V. M. Draviam, and Hiromasa Oku, "High-speed microscopy with an electrically tunable lens to image the dynamics of in vivo molecular complexes," Review of Scientific Instruments, 86, 013707, 2015.

[15] S. Liu and H. Hua, "Extended depth-of-field microscopic imaging with a variable focus microscope objective," Opt. Express 19, 353-362, 2011.

[16] Pawley JB, Masters BR, “Handbook of biological confocal microscopy,” second edition. Opt. Eng. 0001; 35(9):2765-2766.

[17] A. Katsuyuki, Olympus Optical Company, Ltd., Japanese patent 8-292374, November 5, 1996.

6 Summary and future work

6.1 Current Work

This work focuses on design, fabrication and testing of tunable liquid lenses and their use in laparoscopic imaging systems and optical microscopy. The first application that is explored is a multi-camera laparoscopic imaging system.

In summary, we demonstrated a tunable, multi-camera laparoscopic imaging system. Our system directly integrates multiple tunable microcameras with the surgical ports. Preliminary results presented in this paper demonstrate panoramic, large-FoV visualization with enhanced depth perception of the surgical cavity by stitching views from multiple microcameras. A graphical user interface was also developed to enable the surgeons to focus in and out of different features of the surgical scene and control the illumination within the surgical cavity. The integrated trocar-camera assembly offers the surgeon a less-interruptive imaging solution without the need for dedicated imaging ports or inter-port camera navigation during surgery. Our unique approach thus provides promising solutions to several challenges faced by current laparoscopic imaging systems

The second application explored is axial scanning in microscopy using focus-tunable liquid lenses. Herein, proof-of-principle work was demonstrated. The characterization and simulation of the optical tunable microscope setup was presented to achieve an axial scanning range of 1.5mm.

6.2 Future Work

6.2.1 Laparoscopic imaging tool

Future work will focus on optimization of lens design with emphasis on improving resolution and contrast. On the lens design front, different combinations of fixed focus lenses with the tunable liquid lenses will be explored so as to compensate for the spherical and chromatic aberrations of the tunable lenses. Other work will involve development of an image-stitching algorithm optimized for performance in low-light environments as well as customized post-processing techniques for faithful reproduction of the scene. Our future goals also include wireless data transfer, algorithm development for 3D reconstruction, unified user interface design and commercial-grade packaging.

5.2.2. Axial scanning in microscopy using tunable lenses

The tunable liquid lens itself poses high aberrations. Different optical crown and flint-like optical liquid combinations will be substituted in place of water and oil to determine an optimum pair of liquid to minimize aberrations. Future work will also focus on transition from wide field microscopy to confocal microscopy for higher resolution images.

7 Publications

[1] Kanhere, K. Van Grinsven, C.-C. Huang, Y.-S. Lu, J. Greenberg, C. Heise, Y. H. Hu and H. Jiang, “Multi-camera laparoscopic imaging with tunable focusing capability,” IEEE/ASME Journal of Microelectromechanical Systems, vol. 23, no. 6, pp. 1290-1299, 2014.

[2] Kanhere, B. Aldalali, J.A. Greenberg, C.P. Heise, L. Zhang and H. Jiang, "Reconfigurable Micro Camera Array with Panoramic Vision for Surgical Imaging," IEEE/ASME Journal of Microelectromechanical Systems, vol. 22, no. 5, pp. 989-991, 2013.

[3] Aldalali, A. Kanhere, J. Fernandes, C.-C. Huang and H. Jiang, “Fabrication of polydimethylsiloxane microlenses utilizing hydrogel shrinkage and a single molding step,” Micromachines, 5 (2), pp. 275-288, 2014.

[4] Kanhere, K. Van Grinsven, C.-C. Huang, Y.-S. Lu, J. Greenberg, C. Heise, Y. Hu,H. Jiang, “Multi-Camera Laparoscopic Imaging with Tunable Focusing Capability,” *Solid-State Sensors, Actuators, and Microsystems Workshop*, Hilton Head Island, SC, June 8-12, 2014 (Poster).

[5] Kanhere, B. Aldalali, L. Zhang, H. Jiang, "Reconfigurable, panoramic vision micro camera array," *Optical MEMS and Nanophotonics (OMN), 2012 International Conference on* , vol., no., pp.9,10, 6-9 Aug. 2012 (Oral presentation).

[6] Aldalali, A. Kanhere, H. Jiang, "Polydimethylsiloxane microlenses fabricated from liquid-phase photopolymerization and single molding step," *Optical MEMS and Nanophotonics (OMN), 2012 International Conference on* , vol., no., pp.180,181, 6-9 Aug. 2012 (Poster).